ISPRS Journal of Photogrammetry and Remote Sensing 187 (2022) 14–33

Contents lists available at ScienceDirect

ISPRS Journal of Photogrammetry and Remote Sensing

journal homepage: www.elsevier.com/locate/isprsjprs

Taxonomy of seasonal and diurnal clear-sky climatology of surface urban heat island dynamics across global cities

Zihan Liu [a], Wenfeng Zhan [a,b,*], Jiameng Lai [a], Benjamin Bechtel [c], Xuhui Lee [d], Falu Hong [a], Long Li [a], Fan Huang [a], Jiufeng Li [a]

[a] *Jiangsu Provincial Key Laboratory of Geographic Information Science and Technology, International Institute for Earth System Science, Nanjing University, Nanjing, Jiangsu 210023, China*
[b] *Jiangsu Center for Collaborative Innovation in Geographical Information Resource Development and Application, Nanjing 210023, China*
[c] *Department of Geography, Ruhr-University Bochum, 44801 Bochum, Germany*
[d] *School of Forestry and Environmental Studies, Yale University, New Haven, CT 06511, USA*

ARTICLE INFO

Keywords:
Surface urban heat island
Land surface temperature
Thermal remote sensing
Annual temperature cycle
Diurnal temperature cycle
K-means clustering

ABSTRACT

Knowledge of the temporally continuous dynamics of seasonal and diurnal surface urban heat islands (SUHIs) as well as their underlying determinants is crucial to better understand their variations at multiple time scales. Owing to the orbital limitation of satellites, previous studies primarily focused on SUHI dynamics at limited time-nodes, either in a diurnal or seasonal cycle. However, a joint investigation of the continuous dynamics of seasonal and diurnal SUHIs (hereafter referred to as $SUHI_{sea}$ and $SUHI_{diu}$) remains lacking. The comprehensive taxonomy of the patterns of continuous $SUHI_{sea}$ and $SUHI_{diu}$ dynamics across global cities is also not clear. Using satellite-derived land surface temperature (LST) data, we investigated the prevalent patterns of continuous $SUHI_{sea}$ and $SUHI_{diu}$ dynamics across global cities by combining annual and diurnal temperature cycle models and the *k*-means clustering algorithm. Our results showed that: (1) Both $SUHI_{sea}$ and $SUHI_{diu}$ dynamics exhibited six typical patterns including, *single-peak type* (SPT), *single-valley type* (SVT), *peak-valley type* (PVT), *valley-peak type* (VPT), *two-peak type* (TPT), and *two-valley type* (TVT). (2) The daytime $SUHI_{sea}$ dynamics pattern was closely related to the background climate, with SPT and PVT mainly occurring in cities located in the warm temperate and snow zones, SVT and VPT in the arid zone, and TPT and TVT in the equatorial zone. In contrast, the nighttime $SUHI_{sea}$ dynamics pattern depended more on rural land cover type, with SPT, PVT, and TPT mostly occurring in cities surrounded by barren lands with high albedo and SVT, VPT, and TVT in cities surrounded by dense vegetation with low albedo. We also find a significant negative relationship between daytime $SUHI_{sea}$ dynamics and urban-rural contrast in vegetation and between nighttime $SUHI_{sea}$ dynamics and urban-rural contrast in albedo across cities. (3) For $SUHI_{diu}$ dynamics, SPT, PVT, and TVT were mainly located in cities with higher vegetation coverage in rural than in urban areas, while SVT, VPT, and TPT were in cities with higher vegetation coverage in urban areas. The $SUHI_{diu}$ dynamics were found to be synthetically affected by the urban-rural contrast in vegetation and albedo. We consider these findings to be beneficial for deepening the understanding of SUHI dynamics at various time scales.

1. Introduction

The urban heat island (UHI) effect refers to a phenomenon causing higher temperatures over urban surfaces than their rural surroundings (Li et al., 2019; Oke, 1973; Oke et al., 2017; Zhao et al., 2014). The UHI effect has become a global concern in recent years, posing a serious threat to both urban environment and residents (Chakraborty et al., 2020; Clinton and Gong, 2013; Manoli et al., 2019; Peng et al., 2012; Yao et al., 2019). A comprehensive understanding of the UHI effect is, therefore, vital to the design of heat mitigation and human adaptation strategies (Zhou et al., 2014, 2019).

UHIs include canopy UHIs (CUHIs), typically investigated using *in-situ* surface air temperature (SAT), and surface UHIs (SUHIs), usually studied by spaceborne or airborne land surface temperature (LST) (Oke et al., 2017). In recent years, the investigation of SUHIs using satellite-derived LST data has attracted increasing attention because of the

* Corresponding author at: Nanjing University at Xianlin Campus, No. 163 Xianlin Avenue, Qixia District, Nanjing, Jiangsu 210023, China.
E-mail address: zhanwenfeng@nju.edu.cn (W. Zhan).

https://doi.org/10.1016/j.isprsjprs.2022.02.019
Received 8 September 2021; Received in revised form 25 January 2022; Accepted 24 February 2022
Available online 8 March 2022

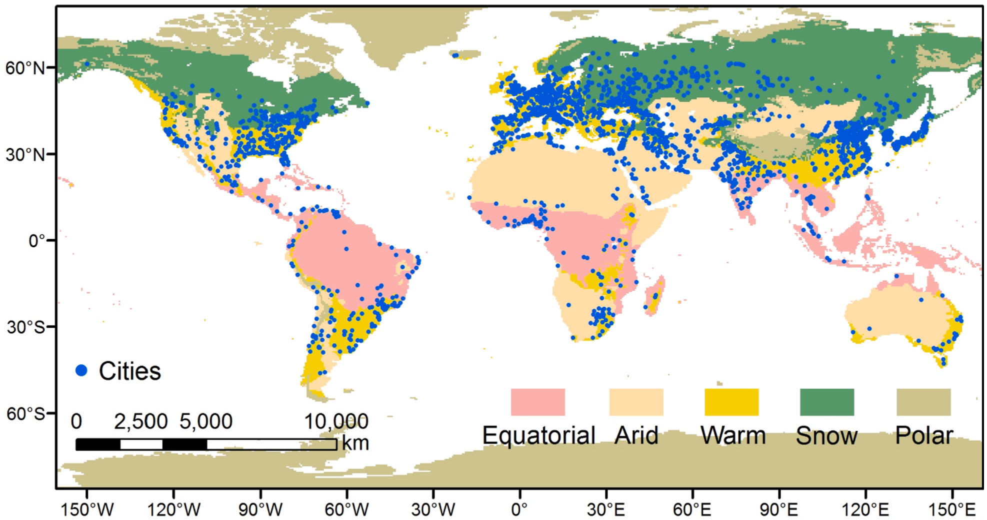

Fig. 1. Distribution of the 2139 cities derived from Natural Earth data (2018). The background colors denote five climate zones, i.e., equatorial, arid, warm temperate, snow, and polar.

availability of large-scale and regular satellite thermal observations (Voogt and Oke, 2003; Yao et al., 2019; Zhou et al., 2019). Many such investigations have focused on SUHI dynamics at both diurnal and seasonal scales (Clinton and Gong, 2013; Manoli et al., 2019; Peng et al., 2012; Streutker, 2003; Tran et al., 2006). However, owing to cloud contamination and satellite orbits, most SUHI dynamics-related efforts have been focused on only one time-node or some typical time-nodes in a diurnal and/or seasonal cycle, and relatively few studies have analyzed the temporally continuous dynamics of the seasonal and diurnal SUHIs ($SUHI_{sea}$ and $SUHI_{diu}$). Thus, the relative lack of the joint analysis of $SUHI_{sea}$ and $SUHI_{diu}$ dynamics has greatly limited the understanding of SUHI variations at multiple time scales.

Nevertheless, to overcome the deficiency of satellite-derived LSTs, several approaches have been proposed recently to better investigate the temporally continuous $SUHI_{sea}$ and $SUHI_{diu}$ dynamics. At the seasonal scale, $SUHI_{sea}$ dynamics have been explored using the *temporal interpolation* techniques such as the annual temperature cycle (ATC) and Fourier series models (Bechtel, 2012; Fu and Weng, 2018; Huang et al., 2016; Manoli et al., 2020; Zhou et al., 2013a, 2016a). At the diurnal scale, $SUHI_{diu}$ dynamics have been investigated either indirectly using the *spatial downscaling* (Bechtel et al., 2012; Sismanidis et al., 2015; Zhou et al., 2013b) and *temporal interpolation* techniques (Huang et al., 2016; Manoli et al., 2020; Zhou et al., 2016a) or directly using the temporally dense thermal observations with a relatively higher spatial resolution obtained from the recently launched geostationary satellites (Chang et al., 2021). Continuous $SUHI_{diu}$ dynamics can be investigated using both the *spatial downscaling* technique, which generates hourly or sub-hourly LST data with a spatial resolution of 1 km or finer, based on the geostationary satellite-derived LSTs (Bechtel et al., 2012; Sismanidis et al., 2015, 2021; Weng and Fu, 2014; Zakšek and Oštir, 2012; Zhou et al., 2013b) and the *temporal interpolation* technique, which produces diurnally continuous LSTs based on limited thermal observations from polar orbiters, such as MODIS and AVHRR, usually with diurnal temperature cycle (DTC) models (Fang et al., 2017; Lai et al., 2018). A very recent study directly employed the LST data with both high spatial and temporal resolutions acquired from the newly launched geostationary satellites (e.g., GOES-R, with spatial and temporal resolutions of 2 km and 5 min, respectively) to investigate the continuous $SUHI_{diu}$ dynamics in Boston, United States (Chang et al., 2021).

Using the above-mentioned approaches, studies have revealed that continuous $SUHI_{sea}$ dynamics vary with the background climate (Manoli et al., 2020). The seasonal hysteresis of SUHI patterns has been shown to be closely related to the time lag between radiation forcing, air temperature, and precipitation and, hence, indirectly to the background climate. For example, observational studies across several typical chosen megacities (including Paris, London, Milan, Madrid, and Nicosia) have shown that $SUHI_{sea}$ dynamics are characterized by a concave-up curve in wet regions with SUHI intensity (SUHII) peaking in summer and a concave-down curve in dry regions with SUHII peaking in spring (Manoli et al., 2020). Nevertheless, even for cities in the same climate zone, the associated $SUHI_{sea}$ dynamics can also be explained by the local surface status, which requires further investigation (Zhou et al., 2013a). Similarly, continuous $SUHI_{diu}$ dynamics (e.g., the timing of peak maximum or minimum SUHIIs) are also related to the background climate and city location (Fang et al., 2017; Sismanidis et al., 2015; Zhou et al., 2013b). For example, SUHII peaks in the day for cities in the wet region, while it drops for cities in the dry region; however, it becomes roughly constant at night in both wet and dry regions (Lai et al., 2018). In addition, the phase shifts among different patterns of $SUHI_{diu}$ dynamics depend significantly on urban geometry and the urban-rural differences in vegetation status, and they are usually higher in the warm season (Lai et al., 2018).

Although great progress has been made in understanding continuous $SUHI_{sea}$ and $SUHI_{diu}$ dynamics, several issues remain to be addressed: First, previous studies have focused on the dynamics of either $SUHI_{sea}$ or $SUHI_{diu}$. A joint investigation of continuous SUHI dynamics at these two timescales remains lacking, restraining an accurate interpretation of SUHI dynamics. Second, previous studies have focused on a few cities or cities with limited types of background climates. With several studies conducted either on the seasonal or diurnal scales, the patterns of continuous $SUHI_{sea}$ and $SUHI_{diu}$ dynamics remain unidentified. With several case cities, it is also difficult and even unfeasible to obtain a holistic taxonomy of the pattern types of continuous $SUHI_{sea}$ or $SUHI_{diu}$ dynamics as well as their relationships with the underlying controls as there is no adequate basis for generalization.

To address these issues, we first investigated continuous $SUHI_{sea}$ and $SUHI_{diu}$ dynamics simultaneously across more than 2000 cities worldwide by combining the ATC and DTC models. Subsequently, we classified all $SUHI_{sea}$ and $SUHI_{diu}$ dynamics into several typical types using the *k*-means clustering algorithm. Finally, the major controls of these dynamics were analyzed. We consider that our taxonomy of $SUHI_{sea}$ and $SUHI_{diu}$ dynamics over global cities should be helpful in enriching the knowledge of SUHI dynamics on multiple timescales.

Table 1
Detailed information of the used satellite and auxiliary data.

	Variable	Abbr.	Temporal/ spatial resolution	Product or Source
Satellite data	Land surface temperature	LST	8-day /1 km	MOD/ MYD11A2
	Enhanced vegetation index	EVI	16-day/1 km	MOD13A2
	Albedo	ALB	16-day/0.5 km	MCD43A3
	Land cover	LC	yearly/0.3 km	CCI-LC
	Nighttime lights	NL	yearly/30-arcsecond	—
Auxiliarydata	Mean air temperature	MAT	monthly/9 km	GLDAS
	Soil moisture	SM	monthly/9 km	GLDAS
	Precipitation intensity	PI	monthly/9 km	GLDAS
	Urban cluster	—	yearly/30 *m*	GUB
	Digital Elevation Model	DEM	yearly/30-arcsecond	GTOPO30

2. Study area and data

2.1. Study area

Our study area included all global urban clusters with an urban area greater than 40 km^2, as determined by the global urban boundary (GUB) data (Li et al., 2020a). According to this criterion, a total of 2027 cities were identified (see Fig. 1). The rural backgrounds of these cities were covered by one or several of the 17 different land cover types based on the International Geosphere-Biosphere Programme (IGBP) classification scheme, and these cities were distributed into five climate zones, including the equatorial, arid, warm temperate, snow, and polar, according to the updated Koppen-Geiger classification scheme (Rubel and Kottek, 2010).

2.2. Data

Both satellite and auxiliary data were used to investigate the SUHI dynamics and their associated controls (Table 1). The satellite data included the MODIS LST, albedo, enhanced vegetation index (EVI), land cover type products from the Climate Change Initiative (CCI) program, and the nighttime lights (NL) data. The details of the data are given in Section 2.2.1. The auxiliary data mainly included the urban cluster, digital elevation model (DEM), and reanalysis data (refer to Section 2.2.2 for the detailed information). The urban cluster and CCI land cover product were used to delineate urban and rural surfaces. The MODIS LST data were used to study the continuous $SUHI_{sea}$ and $SUHI_{diu}$ dynamics, while the remaining data were used to analyze their associated controls.

2.2.1. Satellite data

Three Terra/Aqua MODIS products from 2016 to 2018, including (1) the 8-day composited LST products with a spatial resolution of 1 km (MOD11A2 and MYD11A2), (2) an 8-day composited albedo product with a spatial resolution of 500 m (MCD43A3), and (3) a 16-day composited EVI product with a spatial resolution of 1 km (MOD13A2), were used. Note that here we selected 8-day LST rather daily LST, mainly considering that: the 8-day composition procedure (1) can largely eliminate daily SUHI fluctuations due to variations in synoptic and soil conditions and therefore enable an investigation of SUHI dynamics from a climatological perspective (Lai et al., 2018), (2) can potentially reduce the impacts from data gaps caused by cloud contamination, and (3) can significantly decrease the time to download/process data and therefore increase the global applicability of the associated approach. All datasets were obtained from the Earth Observing System Data and Information System (EOSDIS; https://earthdata.nasa.gov/). The CCI land cover product (2016–2018) were obtained from the European Space Agency (ESA; https://www.esa.int/). The spatial resolution of the CCI land cover product is 300 m, and its overall accuracy is satisfactory according to independent product validations (ESA-European Space Agency, 2017). Both the MODIS albedo and yearly CCI land cover product were resampled to 1 km to match the spatial resolution of the LST data using the bilinear sampling method (i.e., the weighted average method).

The MODIS LST products have been widely validated (Wan, 2008, 2014). They provide four global-coverage LST observations per daily cycle, including two daytime observations at around 01:30 h and 10:30 h and two nighttime observations at approximately 13:30 h and 22:30 h for the local solar time, ensuring the application of the four-parameter DTC model to model the $SUHI_{diu}$ dynamics (Hong et al., 2018, also refer to Section 3.1.2). The MODIS albedo products include both white-sky albedo (WSA) and black-sky albedo (BSA). We used the average of WSA and BSA to represent the actual albedo condition (Román et al., 2010).

The nighttime light (NL) data from 2016 to 2018 were obtained from Li et al. (2020b), which were generated by combining the Defense Meteorological Satellite Program (DMSP)/Operational Linescan System (OLS) and the Visible Infrared Imaging Radiometer Suite (VIIRS) data. The annual NL data with a 30-arcsecond spatial resolution were also resampled to 1 km to match the spatial resolution of the MODIS LSTs using the bilinear sampling method. The NL data, being one of the most commonly used indicators of human activities (Chen et al., 2021b; Du et al., 2021b; Jiang et al., 2021), were employed as a proxy of anthropogenic heat release (AHR) in this study.

2.2.2. Auxiliary data

The GUB data with a spatial resolution of 30 m for 2018 were used to determine urban areas, which can be obtained from a public information-sharing center (http://data.ess.tsinghua.edu.cn). The GUB data are generated from the global artificial impervious area product, and correspond well with the nighttime light data and human interpretation (Li et al., 2020a). Owing to its high quality, this dataset have been widely used in various studies such as the investigation of SUHIs (Du et al., 2021a), urban expansion (Wang et al., 2020), and land use/cover type change (Chen et al., 2021a). The Global 30-arcsecond USGS Digital Elevation Model (GTOPO30) data were obtained from the United States Geological Survey (https://www.usgs.gov/) and resampled to 1 km using the bilinear sampling method to match the resolution of the MODIS LSTs.

We also employed three meteorological variables, including the mean air temperature (MAT), precipitation intensity (PI), and soil moisture (SM) from 2016 to 2018, to examine the controls of SUHI dynamics. These variables were retrieved from the common Global Land Data Assimilation System (GLDAS), a reanalysis dataset available at the Goddard Earth Sciences Data and Information Services Center (GES DISC) (https://disc.sci.gsfc.nasa.gov/datasets/). All these reanalysis data (9 km) were resampled to a resolution of 1 km using the bilinear sampling method to match the resolution of the MODIS LSTs.

3. Methodology

We complied with the following three steps to analyze the taxonomy of $SUHI_{sea}$ and $SUHI_{diu}$ dynamics as well as their determinants: (1) Extraction of the seasonal and diurnal LST dynamics using the ATC and DTC models (refer to Section 3.1), (2) identification of the taxonomy of the typical $SUHI_{sea}$ and $SUHI_{diu}$ dynamics through the derived parameters in the ATC and DTC models using the *k*-means clustering algorithm (Section 3.2), and (3) analysis of the dominant determinants of $SUHI_{sea}$ and $SUHI_{diu}$ dynamics using correlation and linear regression analyses (Section 3.3).

3.1. Extraction of seasonal and diurnal LST dynamics

The seasonal and diurnal LST dynamics were extracted using the ATC

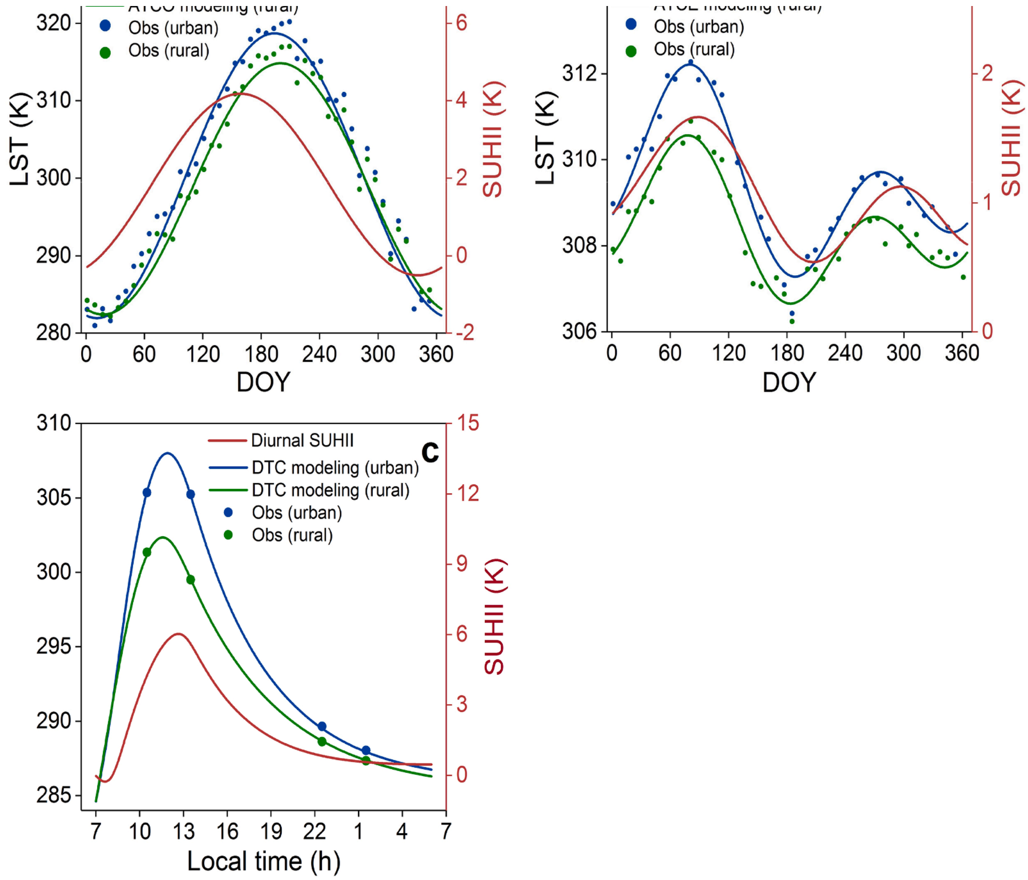

Fig. 2. Illustration of the modeling of the land surface temperature (LST) and surface urban heat island (SUHI) dynamics. (**a**) and (**b**) display the modeling of seasonal LST and SUHI dynamics for the cities outside and within the tropics using the original (ATCO) and enhanced annual temperature cycle (ATCE) models, respectively; and (**c**) displays the modeling of the continuous $SUHI_{diu}$ dynamics using the diurnal temperature cycle (DTC) model. SUHII, Obs, and DOY are the abbreviations for 'SUHI intensity', 'observation', and 'day of year', respectively.

and DTC models, respectively, which can reconstruct the temporally continuous seasonal and diurnal LST dynamics with a limited number of LST observations (Bechtel and Sismanidis, 2017; Duan et al., 2012; Fu and Weng, 2018; Hong et al., 2018). We chose these two types of models because of their physically meaningful parameters, capability to describe LST climatology, and easy global implementation (Bechtel, 2015; Hong et al., 2018).

3.1.1. Extraction of continuous seasonal LST dynamics under clear-sky

We employed both the original ATC model (the ATCO model hereafter) as well as its enhanced version (the ATCE model hereafter) to extract the seasonal LST dynamics (see Fig. 2a). The ATCO model uses a single sinusoidal function plus a constant term (see Fig. 2a), whereas the ATCE model incorporates an additional sinusoidal function, to describe the seasonal LST dynamics (Bechtel, 2011, 2015; Bechtel and Sismanidis, 2017) in the tropics (approx. between 23.5°S and 23.5°N). The ATCO and ATCE models are given by the following equations:

$$T_s(d) = \varphi(C,\ A,\ \omega) = C + A\cdot\sin(2\pi d/365 + \omega) \tag{1}$$

$$T_s^{'}(d) = \varphi^{'}(C^{'},\ A_1,\ A_2,\ \omega_1,\ \omega_2) = C^{'} + A_1\cdot\sin(2\pi d/365 + \omega_1)\ +\ A_2\cdot\sin(4\pi d/365 + \omega_2) \tag{2}$$

where $T_s(d)$ and $T_s'(d)$ are the modeled LSTs based on the ATCO and ATCE models, respectively, on day d within an annual cycle; φ are φ' are the functions of the ATCO and ATCE models, respectively; C, A, and ω of the ATCO model are the annual mean LST, annual LST amplitude, and phase shift relative to the spring equinox, respectively; and C' (equivalent to C) is the annual mean LST, and A_1 (equivalent to A) and A_2 are the amplitudes of the annual and biannual variations, respectively; and ω_1 and ω_2 are the phase shifts. For the ATCO model, ω was defined relative to the spring equinox (Bechtel, 2015) which differs between the northern and southern hemisphere, and it should therefore be revised as $\omega + \pi$ for the southern hemisphere. The ATCO and ATCE models have three (C, A, ω) and five (C, A_1, A_2, ω_1, ω_2) free parameters, respectively, which can be solved by inputting valid LSTs and their associated days of year (DOYs) within an annual cycle using the least squares algorithm.

The LST observations at the Aqua day and night overpass times were used to investigate $SUHI_{sea}$ dynamics, mainly considering that they were acquired around mid-day (i.e., 13:30 h local solar time) and midnight (i.e., 01:30 h local solar time) and, therefore, are more representative for characterizing $SUHI_{sea}$ dynamics for both day and night (Clinton and Gong, 2013; Fu and Weng, 2018). Nevertheless, the DTC model used for extracting $SUHI_{diu}$ dynamics has four controlling parameters, indicating that at least four LST observations per day are needed to solve the DTC model (refer to Section 3.1.2). We therefore incorporated the two Terra-MODIS LST observations to obtain four valid LSTs per day to help investigate the continuous $SUHI_{sea}$ dynamics.

3.1.2. Extraction of continuous diurnal LST dynamics under clear-sky conditions

To extract the continuous diurnal LST dynamics with four inputs per day, we employed an advanced four-parameter DTC model derived from a semi-physical DTC model (the GOT09 model) (Göttsche and Olesen, 2009), which has been shown to be effective for the extraction of continuous diurnal LST and SUHI dynamics with satisfactory accuracy (Hong et al., 2018; Lai et al., 2018). The GOT09_A model uses a sinusoidal function and an exponential function to model LST dynamics for the day and night, respectively (Fig. 2c), given by the following equations:

$$\begin{cases} T_{\mathrm{day}}(t) = T_0 + T_a \dfrac{cos(\theta_z)}{cos(\theta_{z,min})} \cdot exp[0.01 \times (m_{min} - m(\theta_z))], \ t < t_s \\ T_{\mathrm{night}}(t) = T_0 + T_a \dfrac{cos(\theta_{zs})}{cos(\theta_{z,min})} \cdot exp[0.01 \times (m_{min} - m(\theta_{zs}))] \\ \qquad \cdot exp\left[-\dfrac{12}{\pi k}(\theta - \theta_s)\right], \ t \geqslant t_s \end{cases} \tag{3}$$

where $T_{\mathrm{day}}(t)$ and $T_{\mathrm{night}}(t)$ are the LST dynamics for the day and night, respectively; t is the hour of the day; T_0 is the residual temperature around sunrise; T_a is the diurnal temperature amplitude; t_m is the time when the LST reaches its maximum; t_s is the starting time of the free attenuation of LST; θ and θ_z are the thermal hour and solar zenith angles, respectively; θ_s is the thermal hour angle at time t_s, and and $\theta_{z,\ min}$ is the minimum zenith angle at time t_m; θ_{zs} is the thermal zenith angle when θ is equivalent to θ_s; $m(\theta_z)$ and $m_{\min}$ are the relative air mass and the minimum relative air mass at $t = t_s$, respectively; $m(\theta_z)$ is denoted by $m(\theta_{zs})$ when t equals t_s; and k is the attenuation constant of the LST. Detailed descriptions and physical meanings of the constants (i.e., θ, θ_z, θ_s, $\theta_{z,\ min}$, θ_{zs}, $m_{\min}$, k) are available in the paper of Göttsche and Olesen (2009). The GOT09_A model has four free parameters: T_0, T_a, t_m, and t_s (Hong et al., 2018), which were solved using the nonlinear least squares algorithm, analogous to the ATC model and then used to extract the continuous diurnal LST dynamics.

For each pixel within the city, the four valid LSTs were computed through seasonal aggregations (i.e., seasonal mean) of the corresponding daily MODIS transits before being used as the inputs of the GOT09_A model (Hong et al., 2018). This is mainly to eliminate the daily SUHI fluctuations due to variations in synoptic and soil conditions as well as to obtain a seasonal average of the SUHI$_{\mathrm{diu}}$ dynamics from a clear-sky climatological perspective (Lai et al., 2018). As a result, we can obtain four seasonal mean LST observations within a diurnal cycle: [t_1, $T(t_1)$], [t_2, $T(t_2)$], [t_3, $T(t_3)$], and [t_4, $T(t_4)$], where t_1, t_2, t_3, and t_4 are seasonal mean acquisition times, and $T(t_1)$, $T(t_2)$, $T(t_3)$, and $T(t_4)$ are the associated seasonal mean LST composites.

3.2. Identification of the taxonomy of SUHI$_{sea}$ and SUHI$_{diu}$ dynamics

3.2.1. Modeling of SUHI$_{sea}$ and SUHI$_{diu}$ dynamics

The magnitude of SUHI effects was quantified using SUHI intensity (SUHII), typically calculated as the urban-rural difference in LST (Lai et al., 2018; Zhou et al., 2014), which, in turn, requires the delineation of urban and rural areas. For each city, the pixels labelled 'urban and built-up' in the land cover product were used as urban surfaces. The rural areas were defined as the frequently used buffer zones with the sizes equal to the urban areas outside the urban edge (Peng et al., 2012; Zhou et al., 2014). The snow and ice pixels within rural areas were removed because of their extremely low LSTs. The water and permanent wetland pixels within rural areas were also excluded to eliminate the impact of water bodies with a high specific heat capacity (Chakraborty and Lee, 2019). Consistent with previous studies (Chakraborty and Lee, 2019; Lai et al., 2018; Imhoff et al., 2010; Venter et al., 2021), the urban and rural pixels with elevations exceeding $\pm$ 50 m of the median elevation were further removed based on the DEM data to suppress the elevation impacts.

With seasonal and diurnal LST dynamics extracted (Section 3.1) and urban and rural areas delineated, the continuous SUHI$_{\mathrm{sea}}$ (refer to Fig. 2a and 2b) and SUHI$_{\mathrm{diu}}$ (refer to Fig. 2c) dynamics can be calculated using the following equation:

$$I(t) = T_u(t) - T_r(t) \tag{4}$$

where $I(t)$ is the SUHII at time t within a seasonal or diurnal cycle, and $T_u(t)$ and $T_r(t)$ are the mean LSTs for all pixels within urban and rural areas at time t, respectively.

3.2.2. Classification of the patterns of SUHI$_{sea}$ and SUHI$_{diu}$ dynamics

We classified the patterns of continuous SUHI$_{\mathrm{sea}}$ and SUHI$_{\mathrm{diu}}$ dynamics using the following two steps. (1) For each city, we calculated the averages of the associated urban-rural differences in each parameter of the ATC and DTC models and then employed these values as the descriptors of the continuous SUHI$_{\mathrm{sea}}$ and SUHI$_{\mathrm{diu}}$ dynamics. This was plausible because the parameters of these two types of models can directly determine both urban and rural LST dynamics and consequently SUHI dynamics (Fu and Weng, 2018; Huang et al., 2016). (2) We then classified the descriptors of the SUHI$_{\mathrm{sea}}$ and SUHI$_{\mathrm{diu}}$ dynamics (i.e., the parameters of the ATC and DTC models) using the k-means clustering algorithm for all cities (Liu et al., 2018; Zhou et al., 2013a), based on which the typical patterns of SUHI$_{\mathrm{sea}}$ and SUHI$_{\mathrm{diu}}$ dynamics were identified. It should be noted that (1) we used the urban-rural difference in ATCO model derived parameters C, A, and ω as the descriptors of SUHI$_{\mathrm{sea}}$ dynamics outside tropics while used the first three parameters of ATCE (i.e., C, A_1, and ω_1) within the tropics to keep the consistency of the clustering parameters. We kept only these three parameters for the ATCE model because they already contain an adequate amount of information of seasonal LST dynamics for clustering (Bechtel and Sismanidis, 2017). (2) prior to the k-means clustering, each input descriptor was normalized between $-$ 1.0 and 1.0 to suppress the uncertainties caused by scale differences among these parameters. (3) The initial value of K was set from 3 to 10 mainly by referring to previous studies (Zhou et al., 2013a; Lai et al., 2018). (4) The silhouette coefficient (SC) index was applied to determine the most appropriate number of clusters (K) (Zhou et al., 2013a), with a higher value indicating a better cluster result.

With the above-mentioned steps, each city was labeled with a specific SUHI dynamics and then classified according to the labeled patterns. We further calculated the mean pattern of the SUHI dynamics for all cities that were grouped into the same cluster by the k-means clustering algorithm, in order to represent the representative shape of the continuous SUHI dynamics for each cluster.

3.3. Analysis of dominant determinants of SUHI$_{sea}$ and SUHI$_{diu}$ dynamics

The SUHI dynamics have been shown to be related to the background climate, surface properties, and human activities (Peng et al., 2012; Zhao et al., 2014; Zhou et al., 2016b). Here, we included two parameters representing the background climate conditions (i.e., MAT and PI), three surface parameters (i.e., EVI, ALB, and SM), and one human activity parameter (i.e., NL), to investigate the regulation of continuous SUHI$_{\mathrm{sea}}$ and SUHI$_{\mathrm{diu}}$ dynamics by these determinants. We selected these six driving variables, mainly considering that: (1) background climate conditions are largely determined by MAT and PI, which plays an important role in modifying aerodynamic resistance and can therefore impact SUHIs (Zhao et al., 2014; Manoli et al., 2019; Zhou et al., 2016b); (2) surface properties are mainly reflected by the EVI, ALB, and SM, which are directly related to evaporative cooling, solar radiation, and surface heat capacity and can consequently influence SUHIs (Li et al., 2019; Venter et al., 2021; Zhou et al., 2016b); and (3) NL data were used as a proxy for anthropogenic heat emissions due to the wide acceptance by previous studies (Peng et al., 2012; Zhou et al., 2014). Although SUHI dynamics can be impacted by other factors, such as urban structure, topography, and geometry (Li et al., 2020c; Oke et al., 2017; Zhao et al., 2014; Zhou et al., 2017), they were not incorporated in this study, mainly because (1) their seasonal variations are relatively insignificant within an annual cycle, and they are used to determine the overall magnitude of SUHI more than the temporal dynamics of SUHI and (2) they are relatively difficult to obtain for global cities.

In parallel with SUHI dynamics (i.e., urban-rural difference in LST dynamics), we calculated the urban-rural differences in variables, including the ΔEVI, ΔALB, and ΔNL. Due to the coarse resolutions of reanalysis data, it is difficult and even impossible to provide accurate urban-rural contrasts in MAT, PI, and rural SM (SM$_r$) variables across

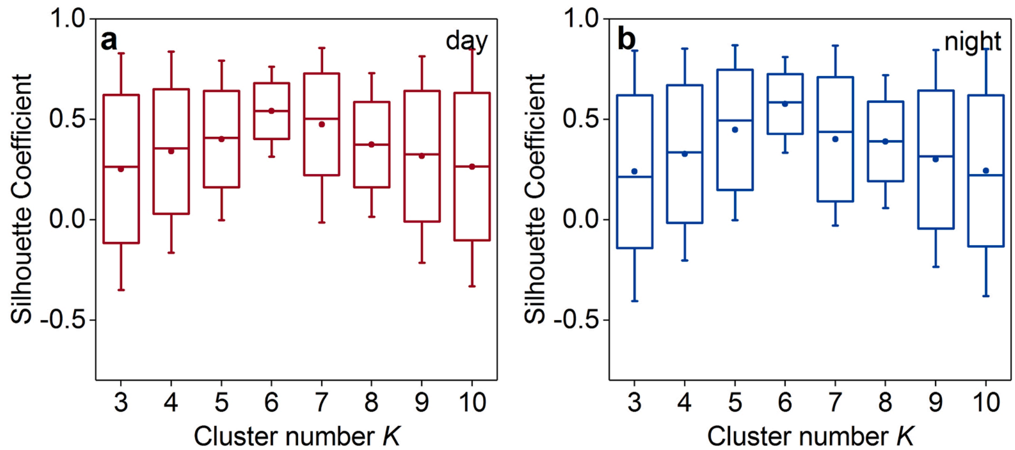

Fig. 3. Variations of the silhouette coefficient of the *k*-mean algorithm depending on cluster number *K* (from 3 to 10) for identifying the typical patterns of continuous seasonal surface urban heat island ($SUHI_{sea}$) dynamics for the daytime (**a**) and nighttime (**b**).

global cities. Consistent with previous studies (Lai et al., 2021b; Peng et al., 2012; Zhou et al., 2016b), the MAT and PI were calculated based on all the available measurements of each city, and the SM_r was calculated as the average of SM over rural areas, in order to represent the background climate and surface conditions of the entire city. We calculated both monthly and seasonal mean values of ΔEVI, ΔALB, ΔNL, MAT, PI, and SM_r for each city. The monthly and seasonal mean ΔNL values were directly set as their yearly values because of the negligible monthly variations in ΔNL (Zhou et al., 2014).

We investigated the relationships between the $SUHI_{sea}$ and $SUHI_{diu}$ dynamics and their potential determinants using a statistical correlation analysis. For $SUHI_{sea}$ dynamics, a correlation analysis between monthly mean SUHII and potential determinants across cities was conducted. Due to the lack of hourly driving variables, it is unable to directly examine the potential determinants of $SUHI_{diu}$ dynamics analogous to the statistical analysis of $SUHI_{sea}$ dynamics. For $SUHI_{diu}$ dynamics, the following two steps were used to analyze their determinants. First, we conducted a correlation analysis between the seasonal mean daytime and nighttime SUHIIs and the potential drivers across cities to identify the $SUHI_{diu}$-related determinants during the day and at night. Note that a seasonal composition procedure was conducted with the purposes of (a) reducing the impacts from data gaps caused by cloud contamination, and (b) eliminating the daily SUHI fluctuations due to variations in synoptic and soil conditions and investigating $SUHI_{diu}$ dynamics from a climatological perspective (Lai et al., 2018). Second, the continuous $SUHI_{diu}$ dynamics with different value groups of the identified $SUHI_{diu}$-related determinants were then further compared to illustrate the different impacts of these $SUHI_{diu}$-related determinants (Lai et al. 2018).

We need to clarify that this study was focused on the $SUHI_{diu}$ dynamics in summer, during which heat mitigation is more important because of the threat posed by SUHI to urban environment and residents (Li et al., 2018; Liu et al., 2018; Oke et al., 2017). Another reason for selecting this season was the significantly greater diurnal variation of SUHII in summer mainly because of the stronger irradiation in this season than in the other seasons (Lai et al., 2018; Manoli et al., 2020). Summer (winter) is defined as the period from June to August (December to February) in the Northern Hemisphere and from December to February (June to August) in the Southern Hemisphere.

4. Results and discussion

4.1. Taxonomy of the seasonal SUHI dynamics

4.1.1. Identified typical patterns of continuous $SUHI_{sea}$ dynamics

The SC variations depending on cluster number *K* (from 3 to 10) are shown in Fig. 3. The results show that the SC reaches a local maximum with the lowest variability, regardless of whether it is day or night, when cluster number *K* is equivalent to six. This indicates that 'six' is the optimal cluster number for the taxonomy of continuous $SUHI_{sea}$ dynamics. Accordingly, six typical daytime and nighttime patterns of continuous $SUHI_{sea}$ dynamics across global cities were identified (Fig. 4; Fig. 5 and Fig. 6). According to the curve shape, these six patterns were termed as *single-peak type* (SPT), *single-valley type* (SVT), *peak-valley type* (PVT), *valley-peak type* (VPT), *two-peak type* (TPT), and *two-valley type* (TVT) (Table 2 and Fig. 4). Such patterns contain three pairs with approximately opposite shapes: SVT versus SPT, VPT versus PVT, and TVT versus TPT. Note that each pattern denotes the average of all cities belonging to the same patterns (Fig. 4). We acknowledge that some cities may exhibit specific patterns of continuous $SUHI_{sea}$ dynamics that differ from the average ones, mostly because of the large bioclimatic discrepancies among cities (Zhou et al., 2013a).

The pattern of daytime continuous $SUHI_{sea}$ dynamics is significantly regulated by the background climate: TPT and TVT mainly occur in the equatorial climate zone, SPT and PVT in warm temperate and snow zones, and SVT and VPT in arid zones (Fig. 7a). Like Manoli et al. (2020), we observed a concave-up shape (peaking in summer, refer to Fig. 4a and Fig. 7) in the wet climate and a concave-down shape (bottoming in summer, Fig. 4c and Fig. 7) in the dry region over several major cities in Europe. The two patterns of $SUHI_{sea}$ dynamics, as shown in Fig. 4a and 4c, directly correspond to the two patterns illustrated by the $SUHI_{sea}$-T_r (T_r denotes the rural LST) plots (Fig. 5a and 5c), as described by Manoli et al. (2020). However, in contrast to a previous finding, we show two similar but slightly different patterns that the $SUHI_{sea}$ dynamics can peak in spring for the wet climate (Fig. 4b) and reach the minimum in spring for the dry climate (Fig. 4d), which correspond to the two elliptical patterns given by the SUHII-rural LST plots (Fig. 5b and 5d). This indicates a phase shift of continuous $SUHI_{sea}$ dynamics between the previously identified patterns, as shown in Fig. 4a and 4c, and the newly identified ones, as shown in Fig. 4b and 4d. Such a phase shift is probably caused by the great variety of urban-rural contrast in LST dynamics resulting from a combination of various surface properties and background climate conditions. This great variety in $SUHI_{sea}$ dynamics has already been revealed partly by previous studies focusing on plentiful cities in Europe (Zhou et al., 2013a). However, in contrast to previous studies, we identified two additional patterns with two peaks or valleys within an annual cycle (i.e., TPT and TVT; Fig. 4e and 4f), which are characterized by the '∞' shape in the SUHII-T_r plots (Fig. 5e and 5f). This suggests that an accurate taxonomy of the $SUHI_{sea}$ dynamics, therefore, requires the incorporation of cities under a great variety of background climates.

At night, TPT and TVT with two peaks/valleys within an annual cycle (refer to Fig. 4k and 4l, corresponding to the SUHII-T_r plots, as shown in

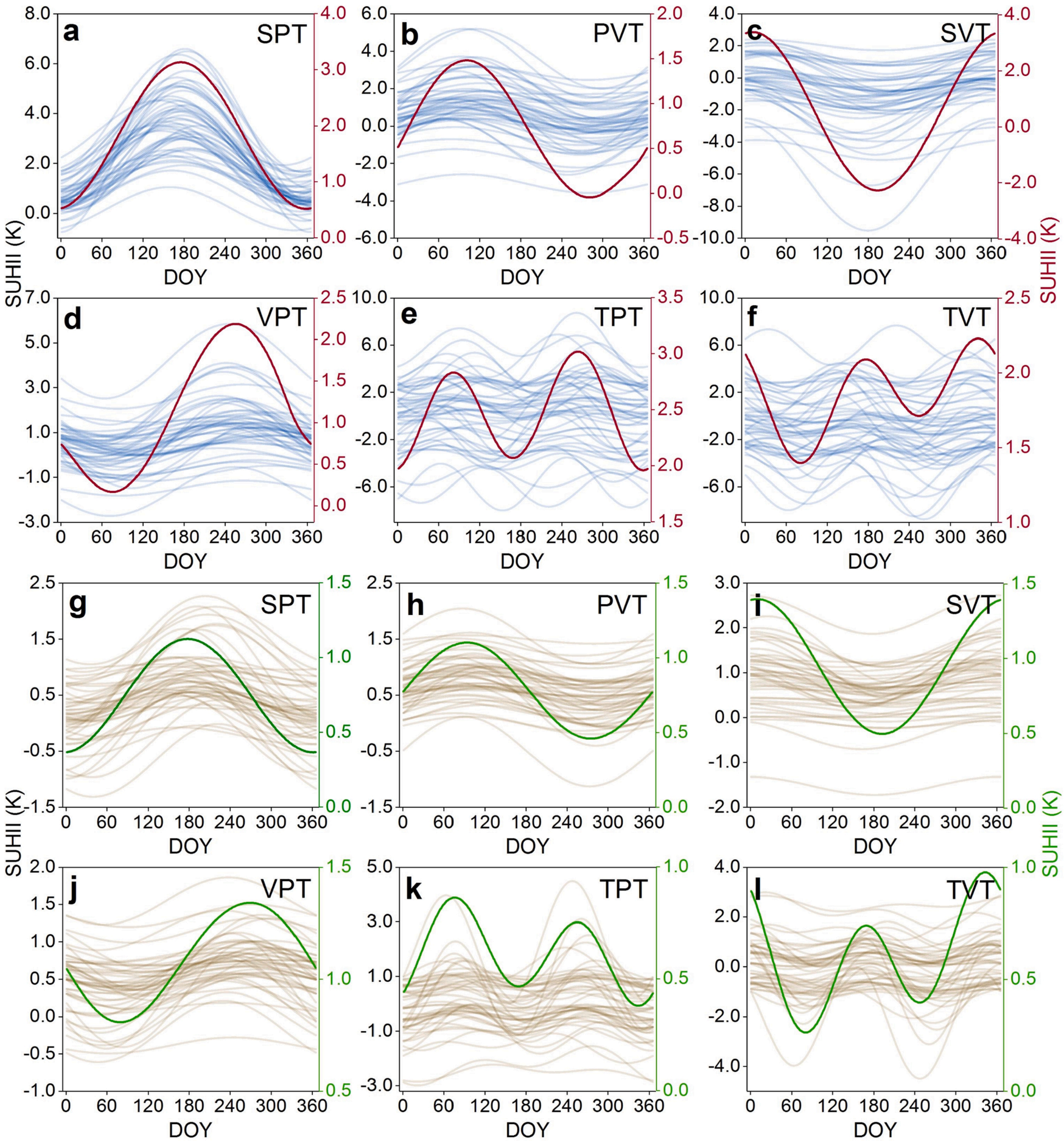

Fig. 4. Six typical patterns of the continuous seasonal surface urban heat island ($SUHI_{sea}$) dynamics over global cities for the daytime (**a**–**f**) and nighttime (**h**–**l**). These patterns include the *single-peak type* (SPT), *peak-valley type* (PVT), *single-valley type* (SVT), *valley-peak type* (VPT), *two-peak type* (TPT), and *two-valley type* (TVT). The description of the shapes of these patterns is given in Table 2. For each panel, the thick line denotes the mean $SUHI_{sea}$ dynamics of all cities grouped in the same category, while the thin lines denote the examples of $SUHI_{sea}$ dynamics in typical cities.

Fig. 6e and 2f, respectively), were more prevalent in the equatorial zone. However, the other four patterns of $SUHI_{sea}$ dynamics, that is, SPT, SVT, PVT, and VPT, all with a single peak/valley within an annual cycle (refer to Fig. 4g–4j, corresponding to the SUHII-T_r plots, as shown in Fig. 6a–2d, respectively), occurred predominantly in warm temperate, snow, and arid climates (Fig. 7b). When compared with the daytime case, the continuous $SUHI_{sea}$ dynamics are less regulated by the background climate, as evidenced by Zhou et al. (2016b). Nevertheless, we further observed that the nighttime continuous $SUHI_{sea}$ dynamics depended strongly on the rural land cover type. For example, SPT and PVT mainly occurred in cities with a rural background of sparse vegetation and bare lands, which possess a relatively higher albedo in urban than in rural surfaces (i.e., $\Delta ALB < 0$). In contrast, SVT and VPT primarily occurred in cities with a rural background of dense vegetation and a relatively lower albedo (i.e., $\Delta ALB > 0$).

4.1.2. *Analysis of the dominant determinants of continuous $SUHI_{sea}$ dynamics*

The daytime $SUHI_{sea}$ dynamics can primarily be explained by the ΔEVI variations (Table A1), as evidenced by a strong negative correlation between the monthly SUHII and ΔEVI dynamics ($r = -0.66$, $p < 0.05$) (Fig. 8a). It is understandable that the increased EVI can enhance evapotranspiration, leading to a cooling effect on surface temperature (Peng et al., 2012; Zhou et al., 2014). An increase in urban EVI

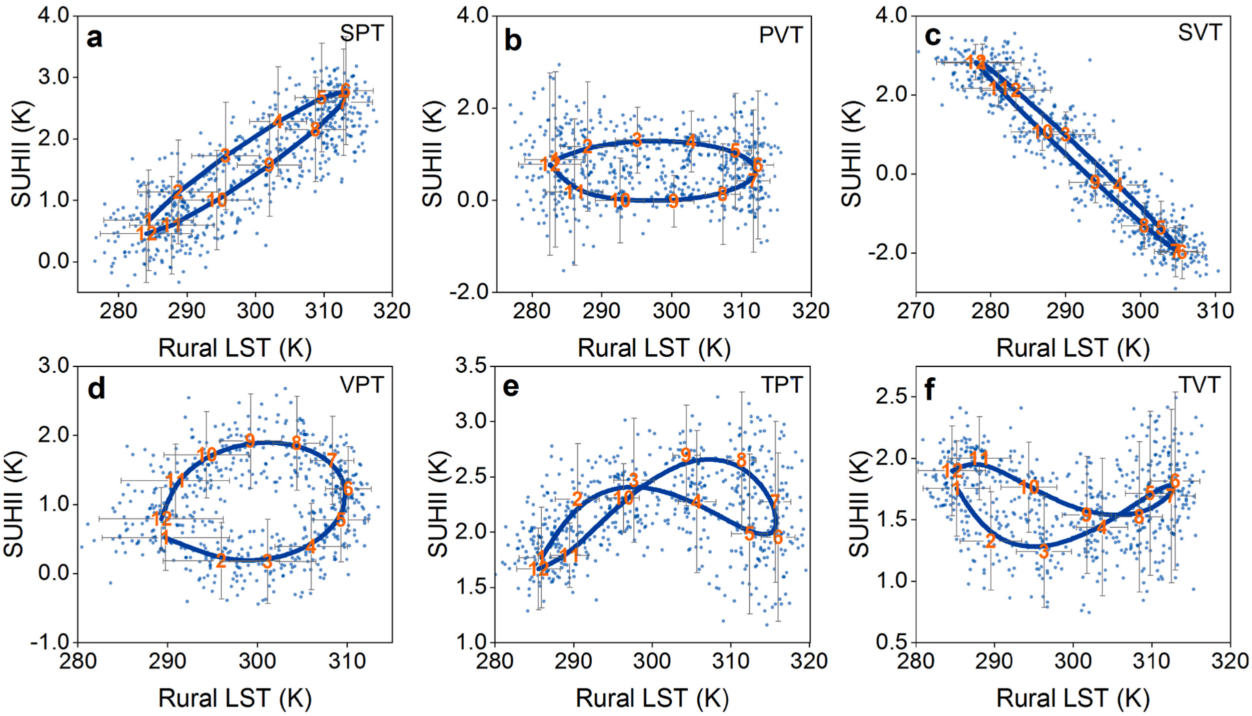

Fig. 5. The six typical patterns of the daytime seasonal surface urban heat island ($SUHI_{sea}$) dynamics as illustrated by the SUHI intensity (SUHII)-rural land surface temperature (T_r) plots. Each dot represents a single city in a certain month; each numerical symbol (i.e., 1–12) represents the mean value of T_r and SUHII for the cities belonging to the same category for a specific month (e.g., '1′ means January); and the bars around each numerical symbol are the associated standard deviations.

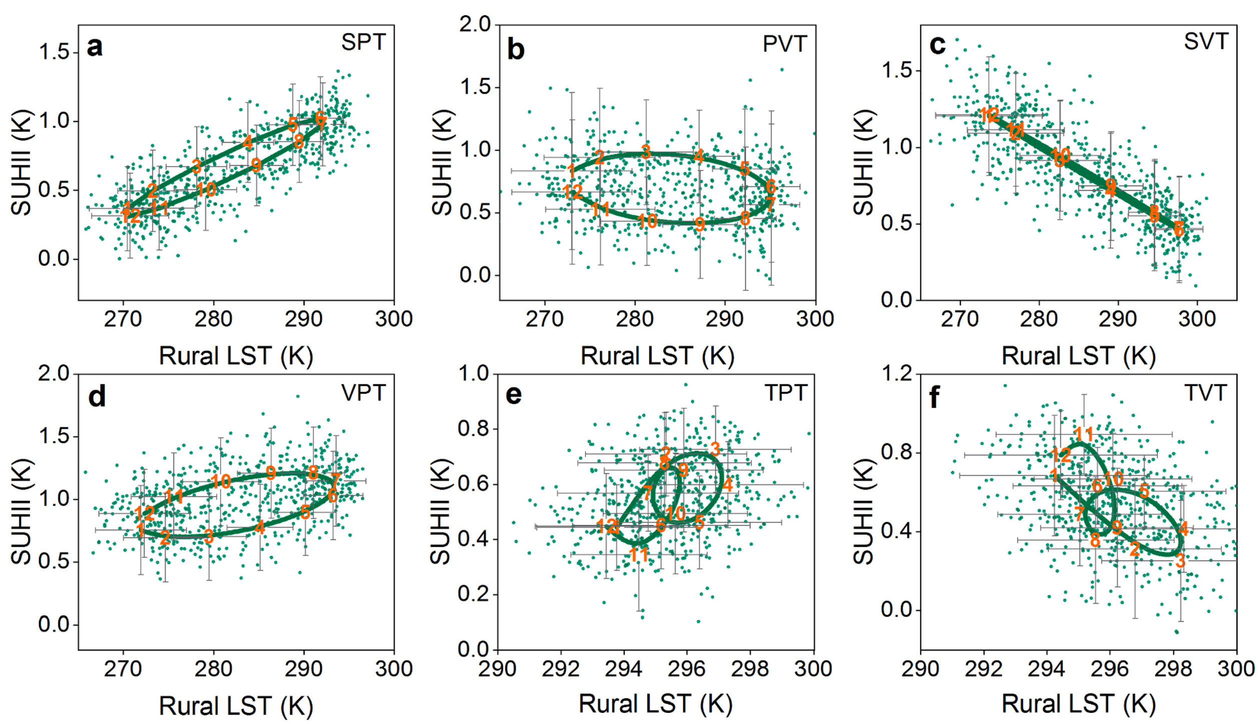

Fig. 6. Six typical patterns of the seasonal surface urban heat island ($SUHI_{sea}$) dynamics as illustrated by the SUHI intensity (SUHII)-rural land surface temperature (T_r) plots, but for the nighttime case.

(associated with an increase in ΔEVI) can reduce the SUHII by enhancing evaporative cooling of urban surfaces (Manoli et al., 2019; Zhou et al., 2014), while an increase in rural EVI (associated with a decrease in ΔEVI) can increase the SUHII by strengthening the rural evaporative cooling effect (Peng et al., 2012; Zhou et al., 2016b). In contrast, the nighttime $SUHI_{sea}$ dynamics were mainly regulated by the ΔALB variations, again with a negative relationship between these two parameters ($r = -0.57, p < 0.05$) (Table A1 and Fig. 8b). A closer look at the monthly variations in SUHII and ΔEVI (or ΔALB) also supports the close relationship between these parameters at the monthly scale (Fig. 9

Table 2
Detailed descriptions on the identified typical patterns of the continuous seasonal surface urban heat island ($SUHI_{sea}$) dynamics for the daytime and nighttime over global cities.

Shape of $SUHI_{sea}$ dynamics	Definition	Descriptions	Spatial distribution for the day	Spatial distribution for the night
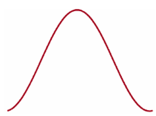	*Single-peak type* (SPT)	A peak in summer and a valley in winter	Warm and snow zones with more vegetation in urban than in rural surfaces	Regions with lower albedo in urban than in rural surfaces
	*Peak-valley type* (PVT)	A peak in spring and a valley in autumn	Warm and snow zones with high population density over urban surfaces	Regions with lower albedo and relatively high population density in urban surfaces
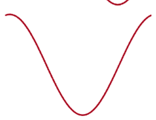	*Single-valley type* (SVT)	A valley in summer and a peak in winter	Arid zones with more vegetation in urban than in rural surfaces	Regions with lower albedo in rural than in urban surfaces
	*Valley-peak type* (VPT)	A valley in spring and a peak in autumn	Arid zones with less precipitation and low temperature	Regions with lower albedo and relatively intensive agricultural practice in rural surfaces
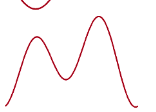	*Two-peak type* (TPT)	Two local peaks in spring and autumn respectively	Equatorial zones with rural surfaces covered by savanna	Equatorial zones with higher albedo in urban than in rural surfaces
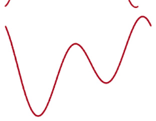	*Two-valley type* (TVT)	Two local valleys in spring and autumn respectively	Equatorial zones with rural surfaces covered by grassland and cropland	Equatorial zones with higher albedo in rural than in urban surfaces

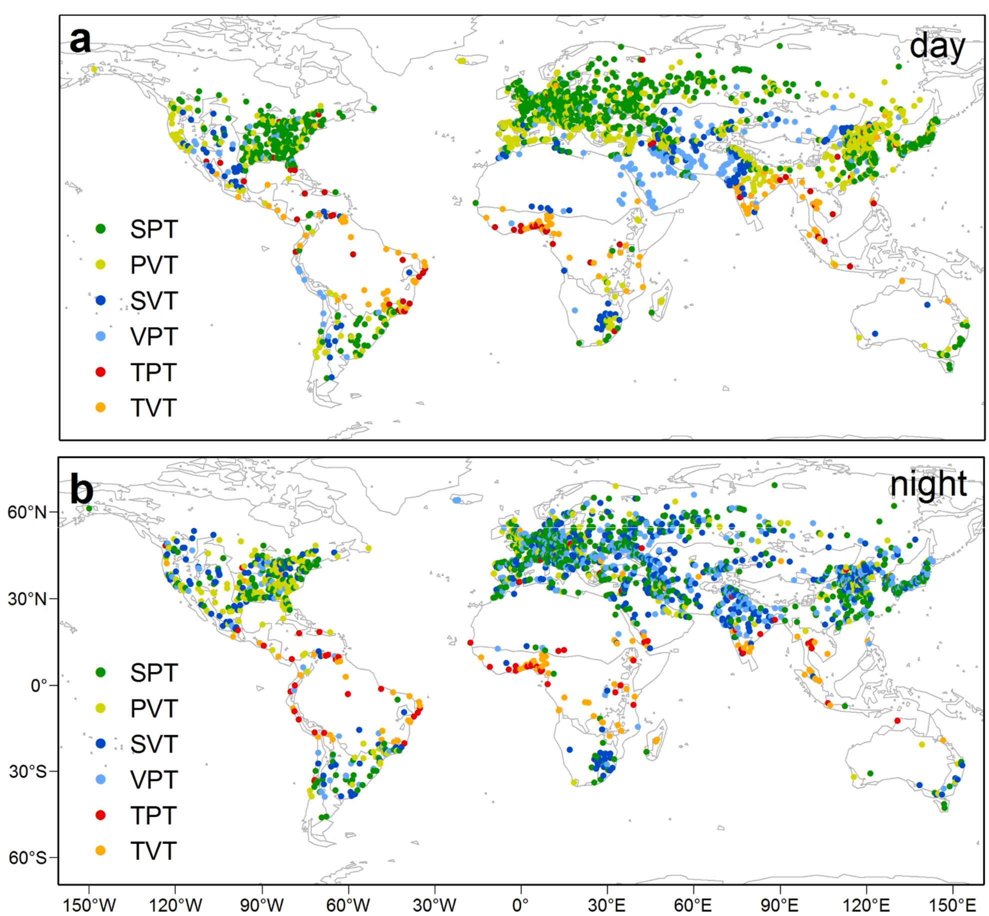

Fig. 7. Spatial distributions of the cities with the six typical patterns of the continuous seasonal surface urban heat island ($SUHI_{sea}$) dynamics for the day (**a**) and night (**b**). (SPT: *single-peak type*; PVT: *peak-valley type*; SVT: *single-valley type*; VPT: *valley-peak type*; TPT: *two-peak type*; TVT: *two-valley type*).

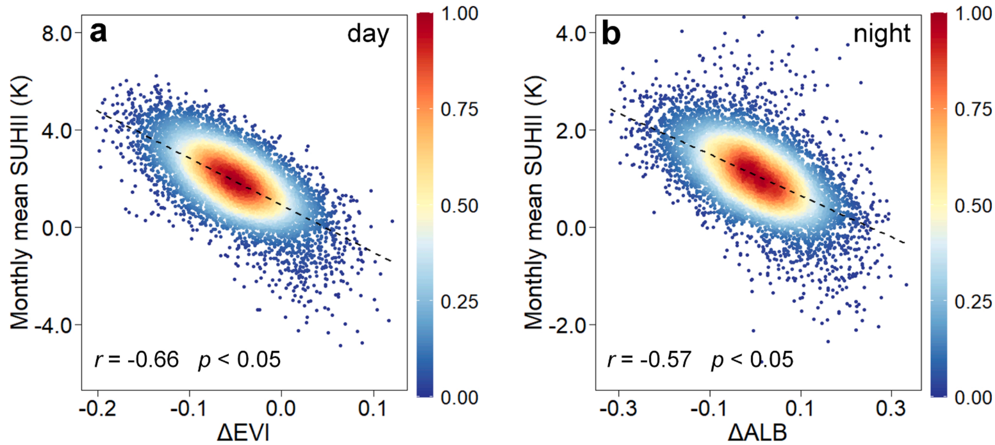

Fig. 8. Relationships between the continuous seasonal surface urban heat island ($SUHI_{sea}$) dynamics and the variations in enhanced vegetation index (ΔEVI) (**a**) and albedo (ΔALB) (**b**). (SUHII: SUHI intensity).

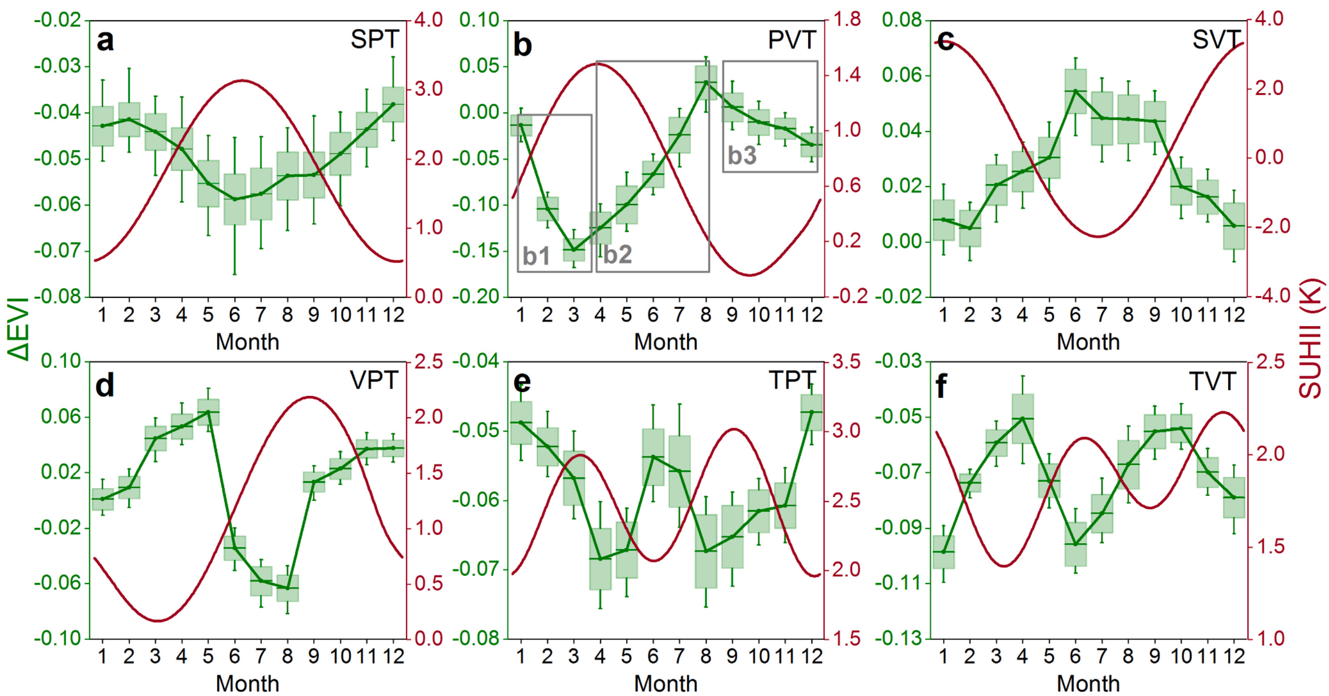

Fig. 9. Relationships between the daytime continuous seasonal surface urban heat island ($SUHI_{sea}$) dynamics (the red lines) and monthly mean enhanced vegetation index (ΔEVI) variations (the green lines), both calculated as the averages of all cities belonging to the same pattern. Rectangles b1, b2, and b3 highlight the dynamics of SUHI intensity (SUHII) and ΔALB in three typical periods, including mid-winter to mid-spring, mid-spring to early autumn, and early autumn to mid-winter, respectively. (For interpretation of the references to colour in this figure legend, the reader is referred to the web version of this article.)

and Fig. 10). We also found a positive relationship between monthly mean SUHII and MAT ($r = 0.32$, $p < 0.05$) and a negative relationship between monthly mean SUHII and PI ($r = -0.34, p < 0.05$ for PI) during the daytime (Table A1). The nighttime $SUHI_{sea}$ dynamics was negatively correlated with the MAT (or PI) ($r = -0.23$, $p < 0.05$ for MAT; $r = -0.21$, $p > 0.05$ for PI).

The results in Fig. 9 show that daytime $SUHI_{sea}$ dynamics are approximately opposite to the seasonal dynamics of ΔEVI. This is understandable because the ΔEVI dynamics directly control the variations in the urban-rural differences in evaporative cooling and hence in SUHII dynamics (Zhou et al., 2014, 2016b). For example, for the SPT pattern mostly occurring in warm and snow climates, the urban EVI is usually less than the rural EVI (ΔEVI < 0; see Fig. 9a), and the $SUHI_{sea}$ dynamics are thus more regulated by the rural than by the urban EVI dynamics; a decrease in ΔEVI (associated with an increase in rural EVI) can strengthen the rural evaporative cooling effect and, therefore, lead to an increase in SUHII. This ensures that the time of the minimum ΔEVI (i.e., maximum rural EVI, around summer) corresponds well with that of the maximum SUHII (Clinton and Gong, 2013; Manoli et al., 2020). For the SVT pattern mostly occurring in the dry climate, the urban EVI, however, is usually greater than rural EVI (ΔEVI > 0; Fig. 9c), indicating that the $SUHI_{sea}$ dynamics should be determined more by urban than rural EVI dynamics. The $SUHI_{sea}$ dynamics in the dry climate, therefore, demonstrate a variation opposite to that in warm and snow climates. Similar to the aforementioned examples, the $SUHI_{sea}$ dynamics shown in Fig. 9b, 9d, 9e, and 9f are closely related to the seasonal dynamics of ΔEVI, which are indirectly regulated by the annual precipitation and temperature cycles (i.e., background climate) and human activities (e.g., cropping and irrigation patterns).

The results in Fig. 10 show that the nighttime $SUHI_{sea}$ dynamics are

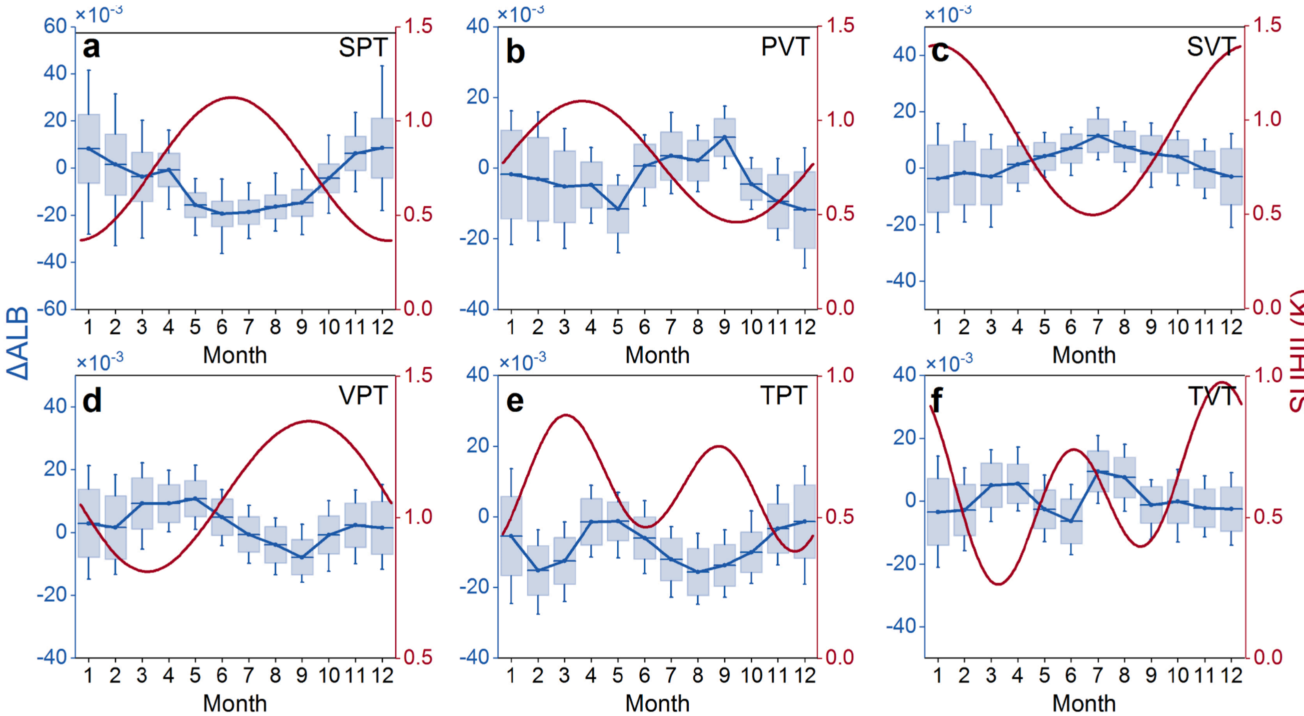

Fig. 10. Relationships between the nighttime continuous seasonal surface urban heat island ($SUHI_{sea}$) dynamics (the red lines) and the monthly mean ΔALB variations (the blue lines), both calculated as the averages of all cities belonging to the same pattern. (For interpretation of the references to colour in this figure legend, the reader is referred to the web version of this article.)

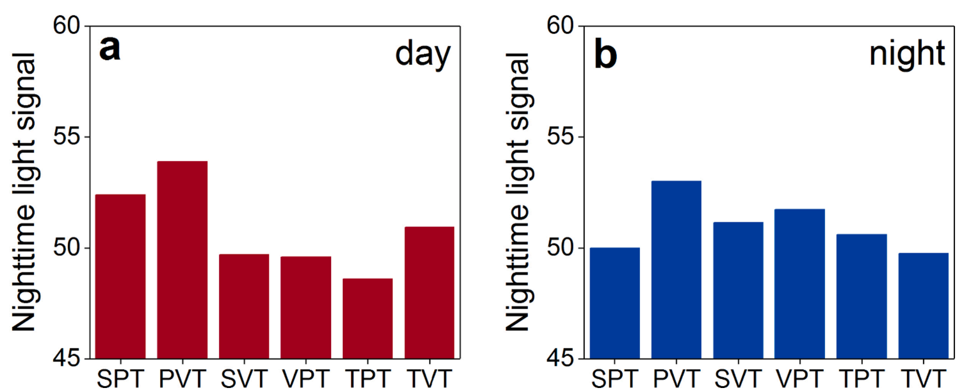

Fig. 11. The nighttime light signal for different patterns of seasonal surface urban heat island ($SUHI_{sea}$) dynamics during the day (**a**) and at night (**b**). (SPT: *single-peak type*; PVT: *peak-valley type*; SVT: *single-valley type*; VPT: *valley-peak type*; TPT: *two-peak type*; TVT: *two-valley type*).

also approximately opposite to the seasonal dynamics of ΔALB. This is mostly because the ΔALB variations determine the dynamics of urban-rural differences in heat storage and accordingly in the nighttime $SUHI_{sea}$ dynamics (Peng et al., 2012; Zhou et al., 2014). For example, for the SPT pattern that mostly appears in cities with a rural background covered by bare soils, the $SUHI_{sea}$ dynamics are more dependent on the urban than on the rural ALB dynamics, and the urban ALB is usually smaller than the rural ALB (ΔALB $<$ 0; see Fig. 10a). For such a pattern, a decrease in ΔALB (usually associated with a decrease in urban ALB) can usually amplify the surface energy trapped during the day and is released at night, leading to an enhancement in SUHII (Peng et al., 2012; Zhou et al., 2014). This enables the minimum ΔALB (i.e., minimum urban ALB around summer) to corresponds well with the maximum SUHII (Fig. 10a). For the SVT pattern that generally occurs in cities with a rural background covered by dense vegetation, the urban ALB, however, is often higher than rural ALB (ΔALB $>$ 0; Fig. 10c), and the $SUHI_{sea}$ dynamics are affected more by rural than urban ALB dynamics. Consequently, the $SUHI_{sea}$ dynamics in cities surrounded by dense vegetation revealed an opposite variation to that in cities surrounded by bare soils (Fig. 10a versus 10c). Like the above-mentioned examples, the $SUHI_{sea}$ dynamics in Fig. 10b, 10d, 10e, and 10f are also closely related to the seasonal variations of ΔALB, which is again indirectly related to surface bioclimate.

Among the six typical patterns of $SUHI_{sea}$ dynamics, three pairs (Section 4.1.1), including the SPT versus PVT (typically in warm temperate and snow climates), SVT versus VPT (mainly in an arid climate), and TPT versus TVT (mostly in the equatorial zone), are for daytime and three similar pairs for nighttime. Nevertheless, hereafter, we were mainly focused on the comparisons of these three pairs during the day, while the comparison for the nighttime case was not itemized to avoid redundancy.

For the first pair of daytime cases, both SPT (accounting for 43.2% of the global cities) and PVT (29.5%) showed a gradual increase in SUHII from mid-winter to mid-spring, which can be largely attributed to more

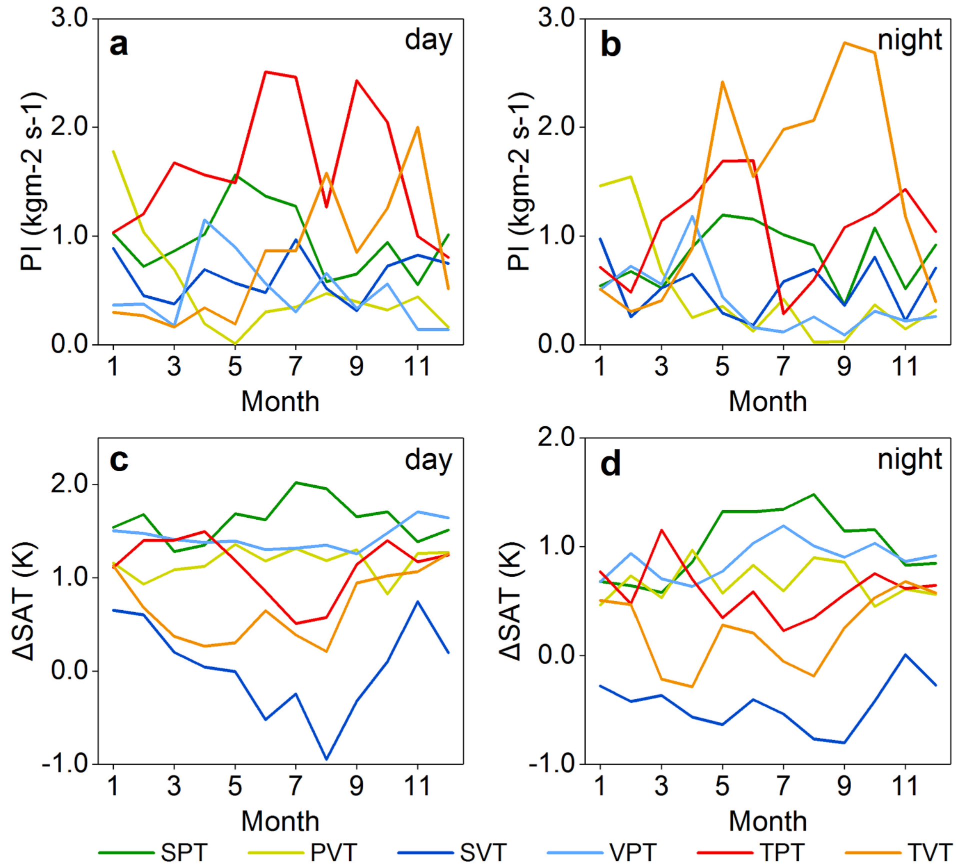

Fig. 12. Monthly variations in precipitation intensity (PI) (**a – b**) and in urban-rural difference of surface air temperature (ΔSAT) (**c – d**) for six typical patterns of the seasonal surface urban heat island ($SUHI_{sea}$) dynamics. (SPT: *single-peak type*; PVT: *peak-valley type*; SVT: *single-valley type*; VPT: *valley-peak type*; TPT: *two-peak type*; TVT: *two-valley type*).

vegetation in rural than in urban surfaces in warm temperatures and snow climates (ΔEVI < 0; Fig. 9a and 9b). From mid-spring to early autumn, SPT was characterized by a concave-up curve with a summer maximum, corresponding well to the concave curve shape of the ΔEVI during this period. In contrast, PVT demonstrated a gradual decreasing trend in SUHII, matching well with the increasing ΔEVI trend probably resulting from crop harvest (Zhou et al., 2016b). Starting from early autumn to mid-winter, the decreasing trend of the SPT was reasonable because of the understandable ΔEVI variation during this period in warm temperatures and snow climates. The increasing SUHII for PVT during this period might have resulted from the increased rural EVI arising from re-cultivated croplands (Zhou et al., 2016b), which led to a reduction in ΔEVI (Fig. 9b). In addition, the cities with PVT are more apt to distribute at high latitudes where there is usually more AHR from domestic heating (Peng et al., 2012). Moreover, the relatively higher AHR for the cities with PVT than those with SPT may contribute to the gradual SUHII increase in winter for the PVT pattern (Fig. 11a).

For the second pair of daytime cases, both SVT (accounting for 8.3% of the global cities) and VPT (9.6%) showed a gradual SUHII decrease from mid-winter to mid-spring, which can be explained by the more vegetation in urban than in rural surfaces in arid climates (ΔEVI > 0; Fig. 9c and 9d). From mid-spring to early autumn, the concave-down shape of the SVT agrees well with the understandable concave-up shape of the ΔEVI variation in arid climates. Conversely, VPT is characterized by a gradual increasing trend, matching well with the decreasing ΔEVI trend that results from the increasing rural EVI because of the gradual growth of natural vegetation and/or cultivated crops in the rural background during this period (Yao et al., 2019; Zhou et al., 2016b). Starting from early autumn to mid-winter, VPT exhibited a gradual decrease in SUHII (Fig. 9d), which can be related to less precipitation, causing a lower rural EVI (a higher ΔEVI accordingly) for VPT, especially when compared with the relatively stable precipitation for SVT (Fig. 12a).

For the third pair of daytime cases, both TPT (accounting for 3.5% of the global cities) and TVT (6.8%) showed two local SUHII peaks or valleys with entirely inverted curve shapes, which can be attributed to seasonal ΔEVI variations characterized by two annual maxima (Fig. 9e and 9f). Such characteristic seasonal ΔEVI variations can further be attributed to the precipitation dynamics exemplified by two annual maxima in the equatorial zone as well as to the impacts of urban-rural temperature differences in vegetation activity (Fig. 12a and 12c; Meng et al., 2020). The inverted curve shapes of these two patterns could be explained by the different rural land cover types (Fig. 13a): the cities with TPT are mostly surrounded by shrublands (57% of the rural background covered by shrublands), whereas the cities with TVT are overwhelmingly surrounded by grasslands and croplands (75%). The growth of shrublands is strongly dependent on precipitation; they start to grow rapidly after an increase in precipitation (Machado et al., 2004; Zhang et al., 2005) and, therefore, reach the ΔEVI peaks just around the occurrence of the precipitation maxima. In contrast, grasslands and croplands take a longer time to respond to precipitation (Machado et al., 2004), thereby producing a phase shift between the maxima of ΔEVI and precipitation. Such a difference in the response of rural vegetation to precipitation likely leads to discrepancies in growth rate in rural vegetation (and accordingly the ΔEVI peaks) and further contributes to different and even entirely opposite curve shapes between TPT and TVT.

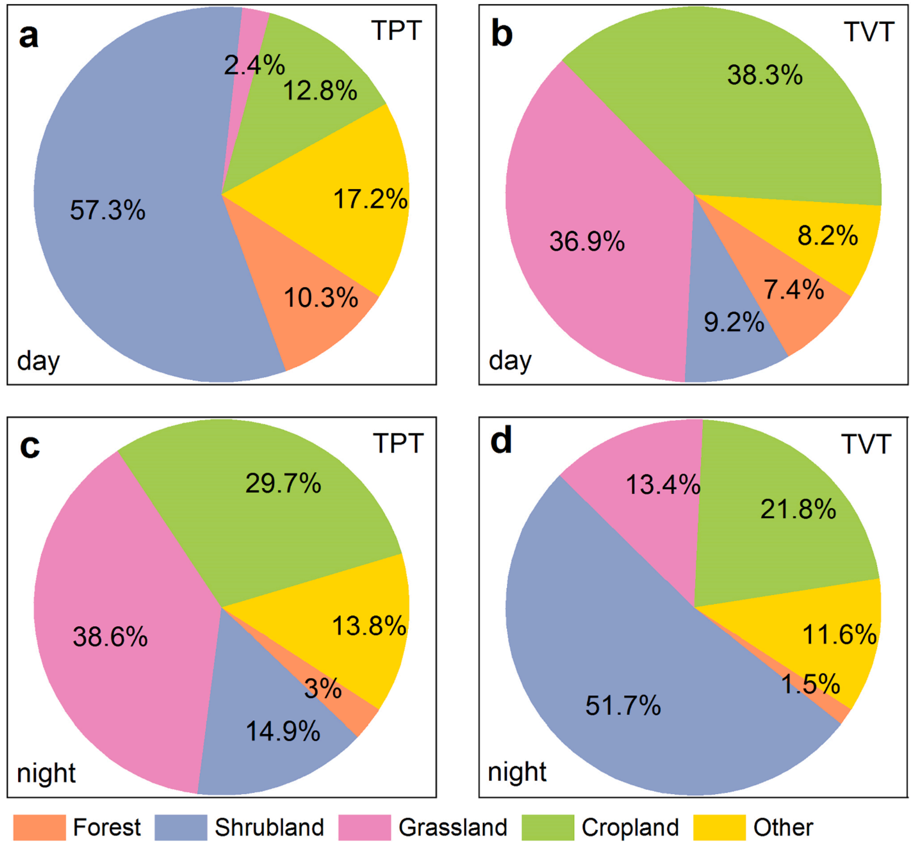

Fig. 13. Distribution of rural land cover types for the cities with the *two-peak type* (TPT) and *two-valley type* (TVT) patterns during the day (**a**) and at night (**b**).

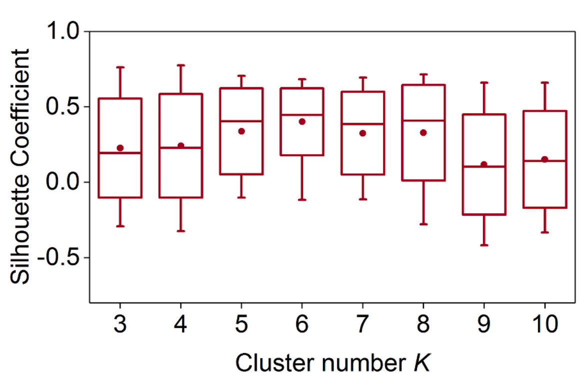

Fig. 14. Variations in the silhouette coefficient of the *k*-mean algorithm depending on cluster number *K* (from 3 to 10) for identifying the typical patterns of continuous $SUHI_{diu}$ dynamics.

4.2. Taxonomy of the diurnal SUHI dynamics

4.2.1. Identified typical patterns of continuous $SUHI_{diu}$ dynamics

According to Fig. 14, the SC values reach a local maximum with the lowest variability when the cluster number *K* is again equivalent to six. Therefore, we identified six typical patterns of continuous $SUHI_{diu}$ dynamics (Fig. 15 and Fig. 16). Like those of the continuous $SUHI_{sea}$ dynamics, we termed these patterns as the SPT, SVT, PVT, VPT, TPT, and TVT (Table 3). These six patterns included three opposing pairs, that is, SPT versus PVT, SVT versus VPT, and TPT versus TVT (see details in Section 4.2.2).

The SPT and PVT patterns are mainly located in warm temperate and snow climates, SVT and VPT in arid climates (Fig. 17), and TPT and TVT across global cities. Among these patterns, the single-peak and single-valley types (i.e., the SPT, SVT, PVT, and VPT) have been reported previously by Lai et al. (2018). Here, we identified two other patterns with two peaks or valleys (TPT and TVT), probably because cities in China are insufficient to provide full insight into the taxonomy of $SUHI_{diu}$ dynamics over global cities.

4.2.2. Analysis of the dominant determinants of continuous $SUHI_{diu}$ dynamics

Similar to previous studies that focused on the spatial dimension (Peng et al., 2012; Zhou et al., 2014, 2016b), our study confirmed a significant negative correlation between daytime SUHII and ΔEVI ($r = -0.50$, $p < 0.05$; see Table A2) and a positive correlation between nighttime SUHII and ΔALB ($r = -0.44$, $p < 0.05$; see Table A2). Note that this statistical analysis differs from that in Section 4.1.2, which was conducted between the $SUHI_{sea}$ dynamics and ΔEVI and ΔALB on the temporal dimension (refer to Section 3.3 for more details on the dominant determinants of $SUHI_{diu}$ dynamics). Studies have indicated that other factors, such as AHR (represented by ΔNL) and SM_r can also affect SUHIIs by regulating energy absorption and release (Zhou et al., 2014; refer to Table A2). Therefore, we mainly analyzed the variations in $SUHI_{diu}$ dynamics depending on these four dominant determinants (ΔEVI, ΔALB, ΔNL, and SM_r).

Fig. 18 shows the variations in continuous $SUHI_{diu}$ dynamics under different values of these four determinants. The results again suggest that $SUHI_{diu}$ dynamics are governed mainly by ΔEVI, but are also impacted by the other three determinants.

For the scenario where urban EVI is lower than rural EVI (ΔEVI < 0) in the daytime, the faster heating of urban impervious surfaces compared with rural dense vegetation forces the rapid SUHII increase after sunrise (Lai et al., 2018), resulting in the SPT pattern (see line a_1 in Fig. 18a). For the scenario where urban EVI is greater than rural EVI (ΔEVI > 0), usually corresponding to cities in an arid climate, the faster

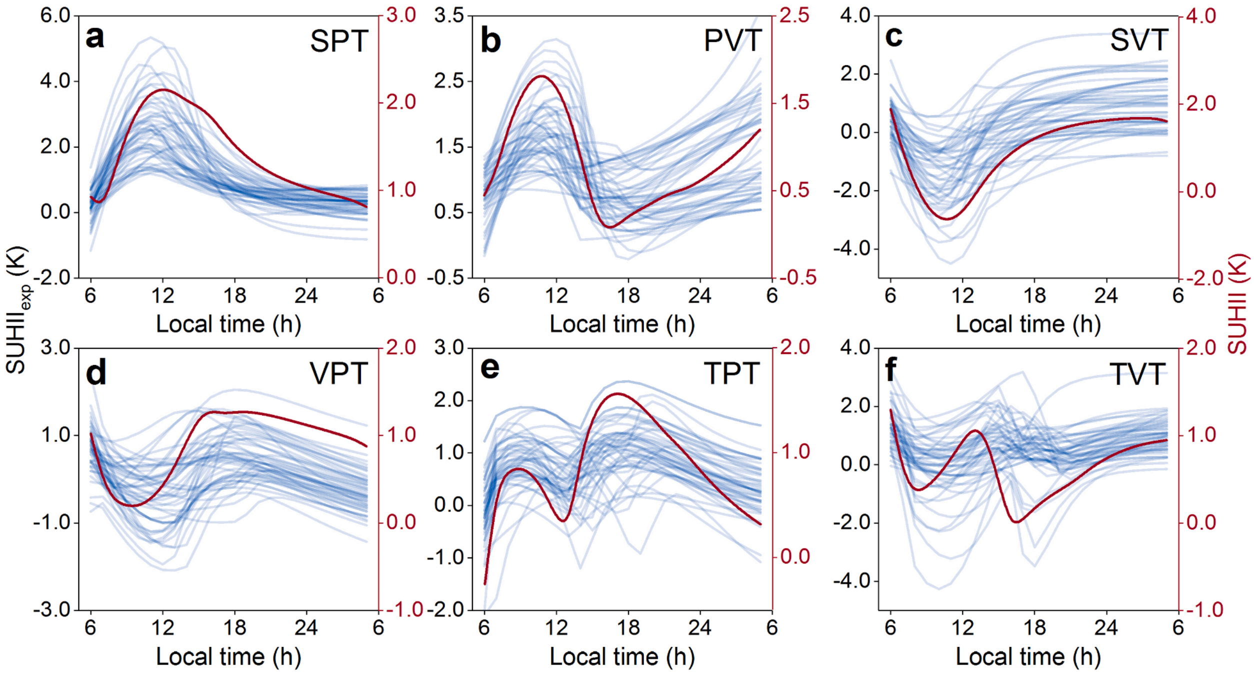

Fig. 15. Six typical patterns of the continuous diurnal surface urban heat island ($SUHI_{diu}$) dynamics over global cities (**a** - **f**). These patterns include the *single-peak type* (SPT), *peak-valley type* (PVT), *single-valley type* (SVT), *valley-peak type* (VPT), *two-peak type* (TPT), and *two-valley type* (TVT), with the descriptions of their shapes given in Table 3. For each panel, the thick line denotes the mean $SUHI_{diu}$ dynamics of all cities grouped in the same category, while the thin lines denote the examples of $SUHI_{diu}$ dynamics in typical cities.

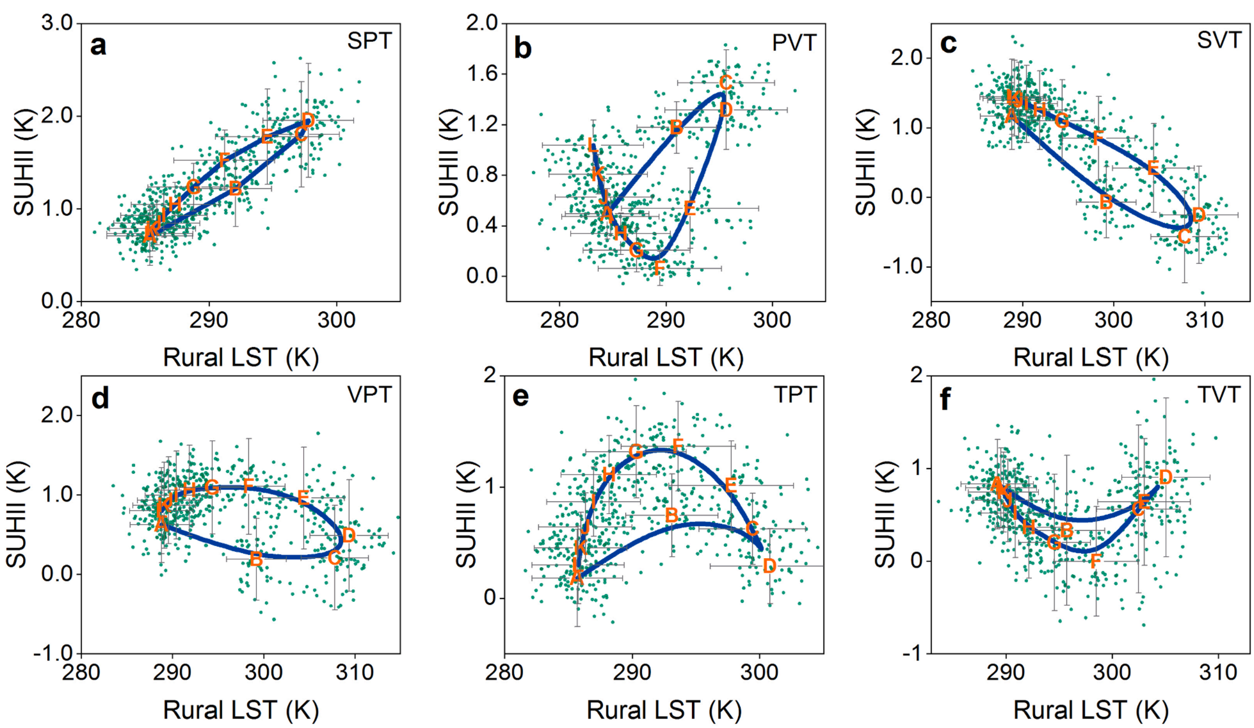

Fig. 16. Six typical patterns of the diurnal surface urban heat island ($SUHI_{diu}$) dynamics as illustrated by the SUHI intensity (SUHII)–rural land surface temperature (T_r) plots. Each dot represents a single city in a certain hour of day; each alphabetical symbol (i.e., A – L) represents the mean value of T_r and SUHII for the cities belonging to the same category for a specific hour of day (e.g., 'A' means the time of sunrise, 'B' denotes 2 h subsequent to sunrise, and so on in the same fashion); and the bars around each alphabetical symbol are the associated standard deviations.

heating of rural bare soils than urban surfaces forces a rapid SUHII decline after sunrise (Lai et al., 2018), leading to the SVT pattern (see line a_2 in Fig. 18a). For the scenario when urban albedo is lower than rural albedo ($\Delta ALB < 0$), usually corresponding to cities in an arid climate surrounded by sparse vegetation and bare lands, the faster nocturnal cooling of rural bare soils, than urban surfaces with more vegetation, canyon effect, and more AHR could enhance the SUHIIs throughout the night (see line b_2 in Fig. 18b). When urban albedo is

Table 3
Detailed descriptions of the identified typical patterns of continuous diurnal surface urban heat island ($SUHI_{diu}$) dynamics over global cities.

Shape of $SUHI_{diu}$ dynamics	Definition	Descriptions	Spatial distribution
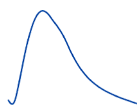	*Single-peak type* (SPT)	A major peak during the day and a gradual decrease at night	Warm and snow climate regions with less vegetation in urban than in rural surfaces
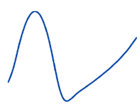	*Peak-valley type* (PVT)	A major peak during the day and a gradual increase at night	Warm and snow climate regions where urban surfaces have less vegetation and high population density than rural surfaces
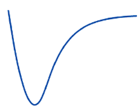	*Single-valley type* (SVT)	A major valley during the day and a gradual increase at night	Arid climate regions with less vegetation in rural than in urban surfaces
	*Valley-peak type* (VPT),	A major valley during the day and a gradual decrease at night	Arid climate regions where rural surfaces have less vegetation and high soil moisture content than urban surfaces
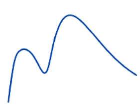	*Two-peak type* (TPT)	Two distinct peaks around noon and early evening	Regions with less vegetation in urban than in rural surfaces
	*Two-valley type* (TVT)	Two distinct valleys around noon and early evening	Regions with more vegetation in urban than in rural surfaces

greater than rural albedo ($\Delta ALB > 0$), which generally corresponds to cities surrounded by dense vegetation, the SUHII continues to decrease at night (see line b_1 in Fig. 18b). This is probably because rural surfaces with dense vegetation can trap more energy during the day and then release it at night, which suppresses the nocturnal cooling of rural surfaces and, therefore, leads to a continuously decreasing SUHII (see line b_1 in Fig. 18b). For the scenario in which the urban-rural contrast in AHR is relatively low (i.e., the ΔNL is low), the daytime SUHII is understandably lower (see line c_1 in Fig. 18c), whereas for the case when ΔNL is relatively high, the nocturnal cooling of urban surfaces is further suppressed owing to the large amount of AHR, which makes the nighttime SUHII variations relatively stable (see line c_2 in Fig. 18c). In contrast, SM_r shows an opposite effect on daytime and nighttime SUHII. Increased SM_r enhances the daytime SUHII as rural moist lands experience slower daytime heating because of their higher heat capacity, which, in turn, decreases the nighttime SUHII by slowing the nocturnal cooling of rural surfaces (see line d_1, Fig. 18d).

For the first pair, both SPT (accounting for 39.0% of the global cities) and PVT (27.5%) presented an increasing first and decreasing later daytime SUHII curve, which should be a result of the greater rural EVI than urban EVI ($\Delta EVI < 0$) for the cities located in the warm temperate and snow climates (Fig. 19a). During the night, a comparatively lower ΔALB can force the nighttime SUHIIs of the PVT pattern to increase because of the negative relationship between ΔALB and nighttime SUHIIs (Fig. 19b and Table A2). The gradual increase in SUHII for PVT could also be explained by the extensive AHR over cities characterized by such a pattern (Fig. 19c).

For the second pair, both SVT (12.9%) and VPT (9.2%) exhibited a decreasing first and increasing later daytime SUHII curve, which can be attributed to the higher urban EVI than rural EVI ($\Delta EVI > 0$), mainly for the cities in the arid climate (Fig. 19a). Instead, the decline in SUHII at night for the VPT pattern was probably related to the relatively higher SM_r when compared with that for SVT, as high SM_r could decrease the nighttime SUHII by slowing the rural cooling (Fig. 19d).

For the third pair, the TPT (6.4%) and TVT (6.0%) patterns showing inverted curve shapes can be closely related to different statuses of ΔEVI, characterized by a positive ΔEVI for TPT and a negative one for TVT (Fig. 19a). The observed perturbations of daytime SUHII for TPT and TVT might have resulted from the combination of the above-mentioned four determinants, including ΔEVI, ΔALB, ΔNL, and SM_r (Allen et al., 2017; Lai et al., 2018, 2021a, 2021b; Oke et al., 2017). Other plausible drivers, such as urban geometry, may also partly contribute to short-term SUHII perturbations by influencing SUHII through the shading effect of urban buildings, which, for instance, can delay the urban heating around sunrise when solar altitudes are low (Allen et al., 2017; Lai et al., 2018).

4.3. Discussion

We performed a joint investigation of the taxonomy of continuous $SUHI_{sea}$ and $SUHI_{diu}$ dynamics over global cities by combining the ATC and DTC models. The patterns of the prevalent $SUHI_{sea}$ and $SUHI_{diu}$ dynamics were identified using the *k*-means clustering algorithm, and the dominant determinants, such as the associated patterns of the continuous $SUHI_{sea}$ and $SUHI_{diu}$ dynamics, were examined. To our

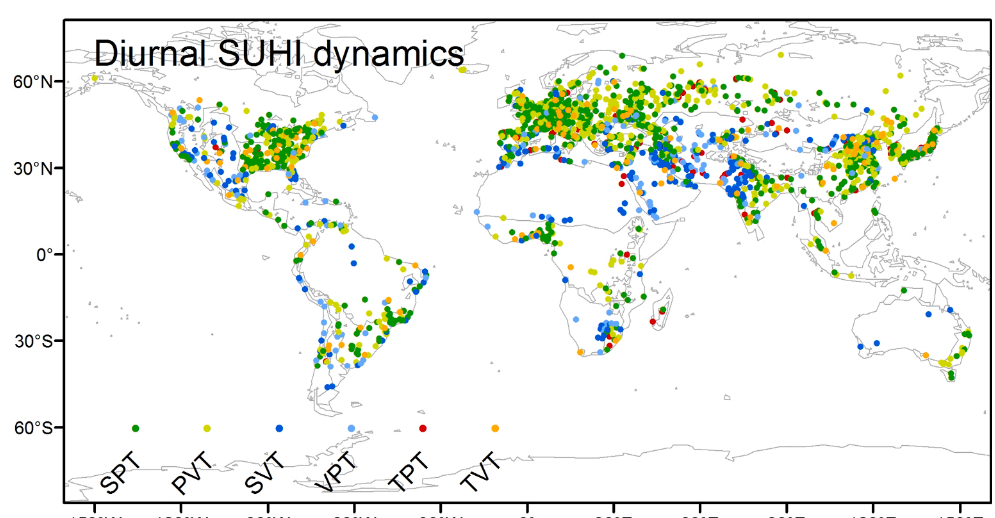

Fig. 17. Spatial distributions of cities with the six typical patterns of continuous diurnal surface urban heat island ($SUHI_{diu}$) dynamics.

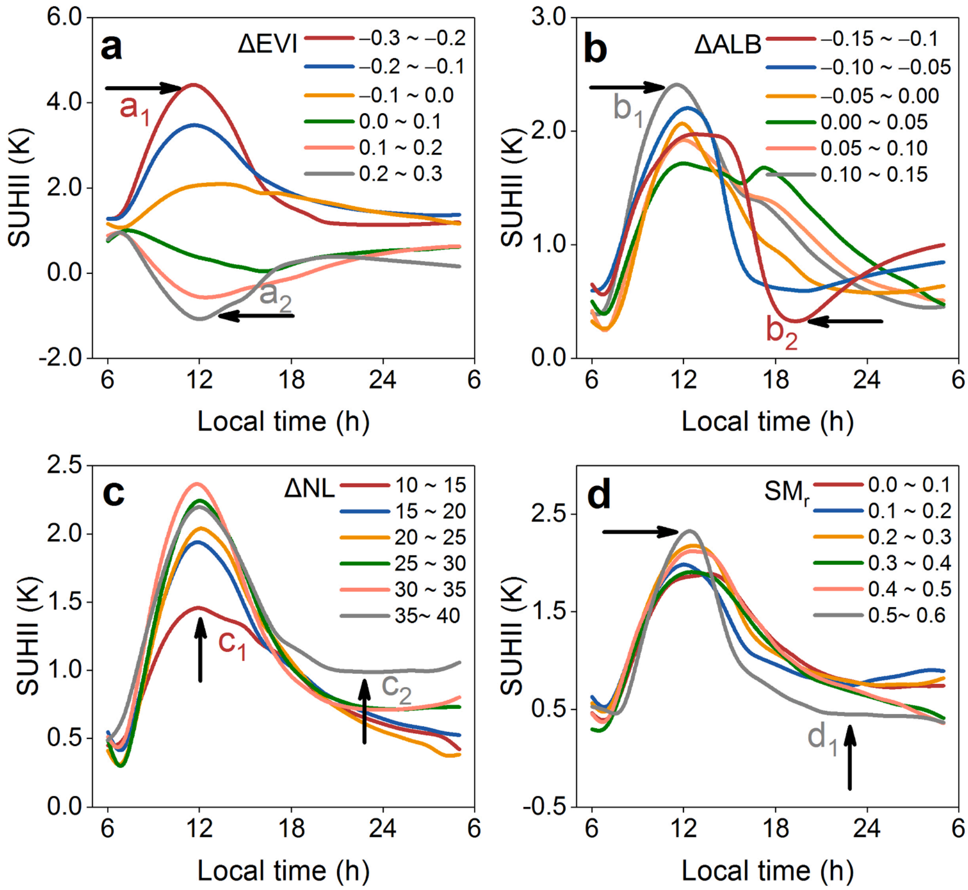

Fig. 18. Variations in continuous diurnal surface urban heat island ($SUHI_{diu}$) dynamics under different values of enhanced vegetation index (ΔEVI) (**a**), albedo (ΔALB) (**b**), ΔNL (**c**), and rural soil moisture (SM_r) (**d**).

knowledge, this is the first study to provide a global perspective on the simultaneous investigation of the $SUHI_{sea}$ and $SUHI_{diu}$ dynamics. Consistent with previous reports (Lai et al., 2018; Zhou et al., 2013a; Manoli et al., 2020), we observed the patterns of $SUHI_{sea}$ and $SUHI_{diu}$ dynamics with one peak or valley within an annual cycle (i.e., SPT, PVT, SVT, and VPT; Fig. 4 and Fig. 15). Yet we found two additional patterns with two peaks or valleys within an annual cycle (i.e., TPT and TVT; Fig. 4 and Fig. 15), which suggests that an accurate taxonomy of the $SUHI_{sea}$ dynamics needs to be conducted from a global perspective. In addition, the simultaneous investigation of $SUHI_{sea}$ and $SUHI_{diu}$ dynamics highlighted that the SUHI dynamics differ by time scale due to the temporal variability of surface-climate conditions and human activities. For example, a closer investigation shows that a certain city may be characterized by the SPT pattern for both $SUHI_{sea}$ and $SUHI_{diu}$ dynamics, while another may not (Fig. A1). Therefore, the results provide an adequate basis for generalization, which is otherwise unobtainable with the data of only a limited number of cities. The results reveal that the patterns (curves) of the identified SUHI dynamics encode several processes and mechanisms that impact SUHII dynamics, which may help in the design of heat mitigation strategies by capturing the possible timing of the mitigation requirement (Lai et al., 2018; Manoli et al., 2020; Zhou et al., 2013a).

However, uncertainties remain, and further efforts are required. First, the ATC and DTC models chosen in this study have been widely used and validated by previous studies (Fu and Weng, 2018; Hong et al., 2018; Huang et al., 2016; Lai et al., 2018). Although the modelling errors of the ATC and DTC models as shown in previous studies are not very low (around 1 to 3 K), we consider that such uncertainties would not largely bias the major conclusions, mostly because we focused on the temporally smoothed seasonal and diurnal patterns (i.e., $SUHI_{sea}$ and $SUHI_{diu}$ dynamics) from a climatological perspective, rather than the day-to-day SUHI fluctuations (generally due to weather and surface changes) from which the modelling errors of the ATC and DTC models are mostly derived. We acknowledge that there exist other ATC models with a relatively higher accuracy by improving the modelling of day-to-day LST fluctuations (Liu et al., 2019). However, such models may yield additional information on short-term LST fluctuations responding to weather and surface changes, which are not necessary to identify the temporally smoothed $SUHI_{sea}$ and $SUHI_{diu}$ dynamics. In addition, in the modeling of continuous SUHI dynamics, similar to previous studies (Lai et al., 2018; Zhou et al., 2016a), the SUHI dynamics extracted by the ATC and DTC models can only represent the scenario of clear-sky climatology, yet the SUHI dynamics are expected to change under overcast conditions (Lai et al., 2018; Zhou et al., 2011). For example, the effect of SUHI may be partly or completely eradicated on windy days (Lai et al., 2021b; Zhou et al., 2011). To acquire accurate SUHI dynamics, more advanced models that can simulate all-weather LSTs are worthy of investigation (Fu et al., 2019; Liu et al., 2019). In addition, the

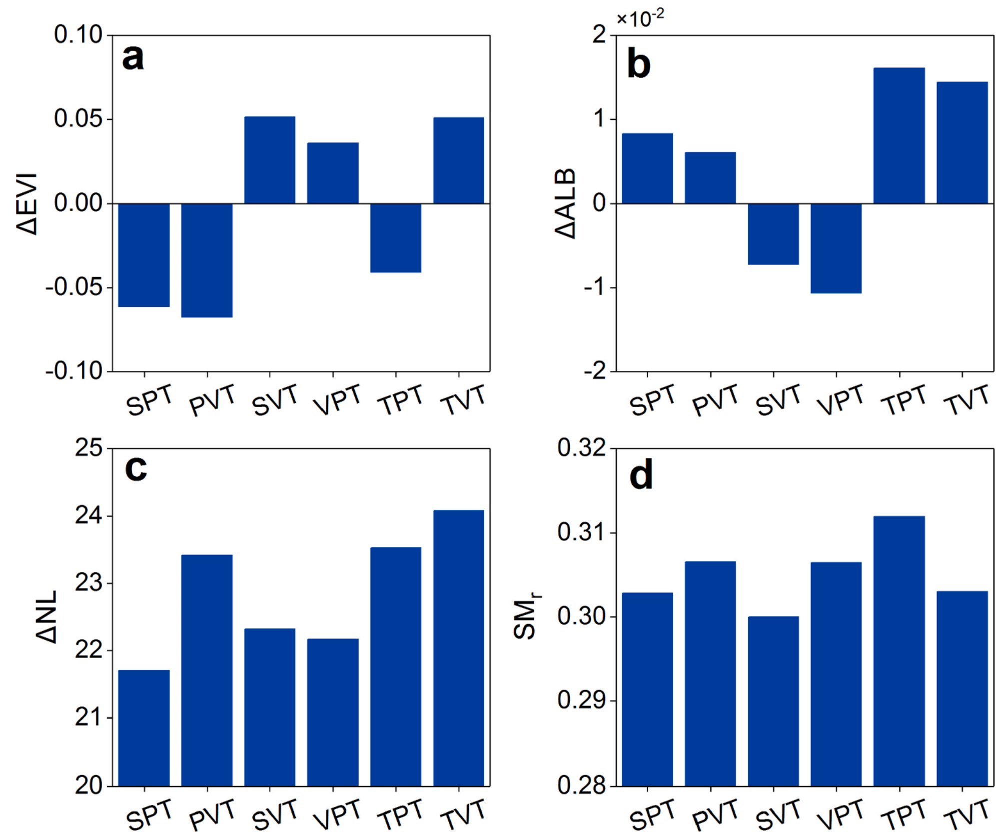

Fig. 19. Mean values of enhanced vegetation index (ΔEVI) (**a**), albedo (ΔALB) (**b**), nighttime lights (ΔNL) (**c**), and rural soil moisture (SM_r) (**d**) for the six patterns of diurnal surface urban heat island ($SUHI_{diu}$) dynamics in summer.

diurnal LST dynamics can be over-simplified by the used DTC model, forcing the associated dynamics into specific predetermined shapes and therefore yielding uncertainties in taxonomy. A previous study has shown that such uncertainties by using parametric models (e.g., the DTC model) are minor by comparing the modelled hourly LSTs with geostationary LSTs over several megacities (Lai et al., 2018), yet more validations with geostationary LSTs over a larger scale may still be necessary to consolidate the obtained taxonomy of the continuous diurnal SUHI dynamics.

Second, during the extraction of typical SUHI dynamics, the typical patterns of SUHI dynamics were determined based on the *k*-means cluster algorithm and SC, which were also employed by previous studies (Rousseeuw, 1987; Zhou et al., 2013a). Therefore, the identified patterns represent the optimal clustering results. The selection of clustering methods may slightly alter the pattern clustering of continuous SUHI dynamics (Liu et al., 2018). Thus, further attempts of algorithm selection are required to improve the clustering accuracy. We also need to clarify that, although the SUHI dynamics were categorized into six groups here, there was no clear boundary among the different patterns: the pattern of an individual city could deviate from any of the six identified patterns because of the specific background climate, topography, and surface properties.

Finally, during the analysis of the determinants of the continuous SUHI dynamics, the coarser resolutions of some auxiliary data were resampled to 1 km to match those of the LST product, which may introduce uncertainties. In addition, we chose only a limited number of determinants to examine the continuous SUHI dynamics, mainly considering their global availability for analysis. We acknowledge that these selected determinants may be inadequate to fully explain the underlying cause of $SUHI_{sea}$ and $SUHI_{diu}$ dynamics. For example, cities with tall buildings should experience a lower SUHI effect because of their higher convection efficiency (Zhao et al., 2014) and larger shadows (Schläpfer et al., 2015), while dense buildings dissipate less heat than rough structures, especially during the night (Grimmond and Oke, 1999; Huang and Wang, 2019; Zhao et al., 2014). These issues highlight the importance of considering auxiliary data with higher spatiotemporal resolutions and involving more variables (e.g., urban density and morphology, cloud coverage, and wind speed) in the future to help investigate the continuous $SUHI_{sea}$ and $SUHI_{diu}$ dynamics. Moreover, we are aware that the analysis of the determinants of SUHI dynamics is only based on a statistical approach, and the captured results remain preliminary. Future studies should conduct a further in-depth analysis of both urban and rural surface energy balance to help disentangle the key drivers of SUHI dynamics (Manoli et al., 2020), especially across global cities under various background climates and city sizes.

5. Conclusion

Previous studies have examined either diurnal or annual SUHI dynamics on single or several time-nodes, but the accurate pattern taxonomy of the continuous SUHI dynamics over these two timescales, especially over global cities, remains unclear. Using the MODIS LSTs and auxiliary data, we investigated both continuous $SUHI_{sea}$ and $SUHI_{diu}$ dynamics across global cities by combining the ATC and DTC models along with the *k*-means clustering algorithm. We further identified the typical patterns of the continuous $SUHI_{sea}$ and $SUHI_{diu}$ dynamics and the associated determinants.

The findings of this study are as follows: (1) Both continuous $SUHI_{sea}$ and $SUHI_{diu}$ dynamics showed six typical patterns, including the SPT, SVT, PVT, VPT, TPT, and TVT. These six patterns included three opposite pairs, with SVT versus SPT, VPT versus PVT, and TVT versus TPT. (2) The daytime $SUHI_{sea}$ dynamics were closely related to the background climate, with SPT and PVT mainly occurring in the warm temperate and snow zones, SVT and VPT in the arid zone, and TPT and TVT in the equatorial zone. The nighttime $SUHI_{sea}$ dynamics were more dependent on the rural land cover type, with SPT, PVT, and TPT mainly occurring in cities surrounded by barren land with high albedo and SVT, VPT, and TVT in cities surrounded by dense vegetation with low albedo. In addition, daytime $SUHI_{sea}$ dynamics were negatively correlated with ΔEVI ($r = -0.66, p < 0.05$), while the nighttime $SUHI_{sea}$ dynamics were negatively correlated with ΔALB ($r = -0.57, p < 0.05$). (3) For $SUHI_{diu}$ dynamics, SPT and PVT mostly appeared in cities with higher vegetation coverage in rural areas than in urban surfaces, while the opposite status of the urban-rural contrast in vegetation coverage led to the occurrence of the SVT, VPT, and TPT. The $SUHI_{diu}$ dynamics were controlled synthetically by the urban-rural contrast in vegetation and albedo. We also found the evidence of other factors, such as AHR and SM_r, regulating the pattern of continuous $SUHI_{diu}$ dynamics. We consider that these findings can advance the understanding of the SUHI dynamics and their associated determinants on multiple timescales; they can also be helpful in designing heat mitigation strategies through the identification of the possible timing of mitigation requirements.

Declaration of Competing Interest

The authors declare that they have no known competing financial interests or personal relationships that could have appeared to influence the work reported in this paper.

Acknowledgments

This study is jointly supported by the National Natural Science Foundation of China (42171306), the National Key Research and Development Programs for Global Change and Adaptation (2017YFA0603604), and the Jiangsu Provincial Natural Science Foundation (BK20180009). We are also very grateful for the financial support from the National Youth Talent Support Program of China.

Appendix

See Fig. A1, Tables A1 and A2

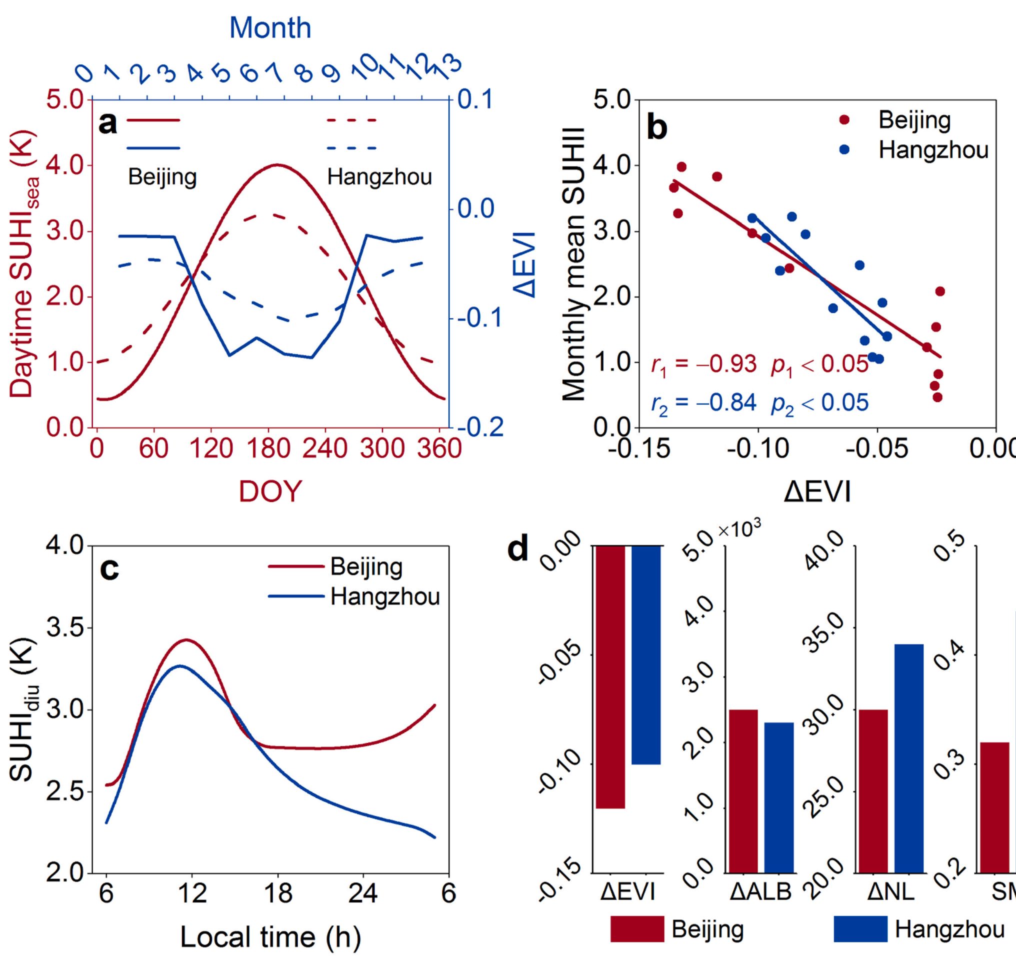

Fig. A1. Comparisons of daytime $SUHI_{sea}$ and $SUHI_{diu}$ dynamics and their determinants in two representative megacities in China (i.e., Beijing and Hangzhou). (**a-b**) Relationships between the $SUHI_{sea}$ dynamics (the red lines) and monthly mean enhanced vegetation index (ΔEVI) variations (the green lines). (**c-d**) Relationships between $SUHI_{diu}$ dynamics and determinants including ΔEVI, albedo (ΔALB), nighttime lights (ΔNL), and rural soil moisture (SM_r).

Table A1
Correlations between the daytime and nighttime seasonal surface urban heat island ($SUHI_{sea}$) dynamics and each determinant across global cities.

Determinants	Seasonal SUHI dynamics			
	Daytime		Nighttime	
	r	*p*	*r*	*p*
ΔEVI	−0.66	< 0.05	0.21	> 0.05
ΔALB	0.14	> 0.05	−0.57	< 0.05
MAT	0.32	< 0.05	−0.23	< 0.05
PI	−0.34	< 0.05	−0.21	> 0.05
SM_r	0.21	> 0.05	−0.19	> 0.05
ΔNL	0.19	> 0.05	0.33	< 0.05

Here, ΔEVI, ΔALB, ΔNL, MAT, and PI represent the urban-rural contrasts in the enhanced vegetation index (EVI), albedo (ALB), nighttime lights (NL), mean air temperature (MAT), rural soil moisture (SM_r), and precipitation intensity (PI), respectively, and *r* and *p* are the statistical correlation coefficient and significance value, respectively.

Table A2
Correlations between daytime (or nighttime) surface urban heat island intensity (SUHII) and each determinant across global cities in summer.

Determinants	Daytime SUHII		Nighttime SUHII	
	r	*p*	*r*	*p*
ΔEVI	−0.48	< 0.05	−0.26	< 0.05
ΔALB	−0.16	> 0.05	−0.41	< 0.05
ΔNL	0.34	< 0.05	0.30	< 0.05
SMr	0.29	< 0.05	−0.27	< 0.05
MAT	−0.16	> 0.05	−0.09	> 0.05
PI	−0.27	< 0.05	−0.15	> 0.05

References

Allen, M.A., Voogt, J.A., Christen, A., 2017. Towards a continuous climatological assessment of urban surface heat islands. In: Urban Remote Sens. Event 1–4.

Bechtel, B., 2011. Multitemporal Landsat data for urban heat island assessment and classification of local climate zones. Urban Remote Sens. Event 129–132.

Bechtel, B., 2012. Robustness of annual cycle parameters to characterize the urban thermal landscapes. IEEE Geosci. Remote Sens. Lett. 9 (5), 876–880.

Bechtel, B., Zakšek, K., Hoshyaripour, G., 2012. Downscaling land surface temperature in an urban area: a case study for Hamburg. Germany. Remote Sens. 4 (10), 3184–3200.

Bechtel, B., 2015. A new global climatology of annual land surface temperature. Remote Sens. 7 (3), 2850–2870.

Bechtel, B., Sismanidis, P., 2017. Time series analysis of moderate resolution land surface temperatures. In: Weng, Q. (Ed.), Remote Sensing Time Series Image Processing. CRC Press, pp. 111–142.

Chakraborty, T., Lee, X., 2019. A simplified urban-extent algorithm to characterize surface urban heat islands on a global scale and examine vegetation control on their spatiotemporal variability. Int. J. Appl. Earth Obs. Geoinf. 74, 269–280.

Chakraborty, T., Hsu, A., Manya, D., Sheriff, G., 2020. A spatially explicit surface urban heat island database for the United States: characterization, uncertainties, and possible applications. ISPRS J. Photogramm. Remote Sens. 168, 74–88.

Chang, Y., Xiao, J., Li, X., Frolking, S., Zhou, D., Schneider, A., Weng, Q., Yu, P., Wang, X., Li, X., Liu, S., Wu, Y., 2021. Exploring diurnal cycles of surface urban heat island intensity in Boston with land surface temperature data derived from GOES-R geostationary satellites. Sci. Total Environ. 763, 144224.

Chen, B., Tu, Y., Song, Y., Theobald, D.M., Zhang, T., Ren, Z., Li, X., Yang, J., Wang, J., Wang, X.i., Gong, P., Bai, Y., Xu, B., 2021a. Mapping essential urban land use categories with open big data: Results for five metropolitan areas in the United States of America. ISPRS J. Photogramm. Remote Sens. 178, 203–218.

Chen, T., Hui, E.C.M., Tu, Y., Lang, W., 2021b. Growth or Shrinkage: Discovering development patterns and planning strategies for cross-border areas in China. J. Urban Plan. Dev. 147 (4), 05021046. https://doi.org/10.1061/(ASCE)UP.1943-5444.0000761.

Clinton, N., Gong, P., 2013. MODIS detected surface urban heat islands and sinks: Global locations and controls. Remote Sens. Environ. 134, 294–304.

Du, H., Zhan, W., Liu, Z., Li, J., Li, L., Lai, J., Miao, S., Huang, F., Wang, C., Wang, C., Fu, H., Jiang, L.u., Hong, F., Jiang, S., 2021a. Simultaneous investigation of surface and canopy urban heat islands over global cities. ISPRS J. Photogramm. Remote Sens. 181, 67–83.

Du, X., Shen, L., Wong, S.W., Meng, C., Yang, Z., 2021b. Night-time light data based decoupling relationship analysis between economic growth and carbon emission in 289 Chinese cities. Sustain. Cities Soc. 73, 103119. https://doi.org/10.1016/j.scs.2021.103119.

Duan, S.-B., Li, Z.-L., Wang, N., Wu, H., Tang, B.-H., 2012. Evaluation of six land-surface diurnal temperature cycle models using clear-sky in situ and satellite data. Remote Sens. Environ. 124, 15–25.

ESA-European Space Agency (2017). Land Cover CCI Product User Guide Version 2. Tech. Rep. Available at: maps.elie.ucl.ac.be/CCI/viewer/download/ESACCI-LC-Ph2-PUGv2_2.0.pdf.

Fang, Y., Zhan, W., Huang, F., Gao, L., Quan, J., Zou, Z., 2017. Hourly variation of surface urban heat island over the Yangtze River Delta urban agglomeration. Adv. Earth Sci. 32 (2), 187–198.

Fu, P., Xie, Y., Weng, Q., Myint, S., Meacham-Hensold, K., Bernacchi, C., 2019. A physical model-based method for retrieving urban land surface temperatures under cloudy conditions. Remote Sens. Environ. 230, 111–191.

Fu, P., Weng, Q., 2018. Variability in annual temperature cycle in the urban areas of the United States as revealed by MODIS imagery. ISPRS J. Photogramm. Remote Sens. 146, 65–73.

Göttsche, F.-M., Olesen, F.-S., 2009. Modelling the effect of optical thickness on diurnal cycles of land surface temperature. Remote Sens. Environ. 113 (11), 2306–2316.

Grimmond, C.S.B., Oke, T.R., 1999. Aerodynamic properties of urban areas derived from analysis of surface form. J. Appl. Meteorol. 38 (9), 1262–1292.

Hong, F., Zhan, W., Göttsche, F.-M., Liu, Z., Zhou, J.i., Huang, F., Lai, J., Li, M., 2018. Comprehensive assessment of four-parameter diurnal land surface temperature cycle models under clear-sky. ISPRS J. Photogramm. Remote Sens. 142, 190–204.

Huang, F., Zhan, W., Voogt, J., Hu, L., Wang, Z., Quan, J., Ju, W., Guo, Z., 2016. Temporal upscaling of surface urban heat island by incorporating an annual temperature cycle model: A tale of two cities. Remote Sens. Environ. 186, 1–12.

Huang, X., Wang, Y., 2019. Investigating the effects of 3D urban morphology on the surface urban heat island effect in urban functional zones by using high-resolution remote sensing data: A case study of Wuhan, Central China. ISPRS J. Photogramm. Remote Sens. 152, 119–131.

Imhoff, M.L., Zhang, P., Wolfe, R.E., Bounoua, L., 2010. Remote sensing of the urban heat island effect across biomes in the continental USA. Remote Sens. Environ. 114 (3), 504–513.

Jiang, S., Zhang, Z., Ren, H., Wei, G., Xu, M., Liu, B., 2021. Spatiotemporal Characteristics of Urban Land Expansion and Population Growth in Africa from 2001 to 2019: Evidence from Population Density Data. Int. J. Appl. Earth Obs. Geoinf. 10 (9), 584.

Lai, J., Zhan, W., Huang, F., Voogt, J., Bechtel, B., Allen, M., Peng, S., Hong, F., Liu, Y., Du, P., 2018. Identification of typical diurnal patterns for clear-sky climatology of surface urban heat islands. Remote Sens. Environ. 217, 203–220.

Lai, J., Zhan, W., Quan, J., Bechtel, B., Wang, K., Zhou, J.i., Huang, F., Chakraborty, T., Liu, Z., Lee, X., 2021a. Statistical estimation of next-day nighttime surface urban heat islands. ISPRS J. Photogramm. Remote Sens. 176, 182–195.

Lai, J., Zhan, W., Voogt, J., Quan, J., Huang, F., Zhou, J.i., Bechtel, B., Hu, L., Wang, K., Cao, C., Lee, X., 2021b. Meteorological controls on daily variations of nighttime surface urban heat islands. Remote Sens. Environ. 253, 112198. https://doi.org/10.1016/j.rse.2020.112198.

Li, D., Liao, W., Rigden, A.J., Liu, X., Wang, D., Malyshev, S., Shevliakova, E., 2019. Urban heat island: Aerodynamics or imperviousness? Sci. Adv. 5 (4), eaau4299.

Li, H., Meier, F., Lee, X., Chakraborty, T., Liu, J., Schaap, M., Sodoudi, S., 2018. Interaction between urban heat island and urban pollution island during summer in Berlin. Sci. Total Environ. 636, 818–828.

Li, X., Gong, P., Zhou, Y., Wang, J., Bai, Y., Chen, B., Hu, T., Xiao, Y., Xu, B., Yang, J., Liu, X., Cai, W., Huang, H., Wu, T., Wang, X.i., Lin, P., Li, X., Chen, J., He, C., Li, X., Yu, L.e., Clinton, N., Zhu, Z., 2020a. Mapping global urban boundaries from the global artificial impervious area (GAIA) data. Environ. Res. Lett. 15 (9), 094044. https://doi.org/10.1088/1748-9326/ab9be3.

Li, X., Zhou, Y., Zhao, M., Zhao, X., 2020b. A harmonized global nighttime light dataset 1992–2018. Sci. Data 7 (1), 1–9.

Li, Y., Schubert, S., Kropp, J.P., Rybski, D., 2020c. On the influence of density and morphology on the Urban Heat Island intensity. Nat. Commun. 11 (1), 1–9.

Liu, H., Zhan, Q., Yang, C., Wang, J., 2018. Characterizing the spatio-temporal pattern of land surface temperature through time series clustering: based on the latent pattern and morphology. Remote Sens. 10 (4), 654.

Liu, Z., Zhan, W., Lai, J., Hong, F., Quan, J., Bechtel, B., Huang, F., Zou, Z., 2019. Balancing prediction accuracy and generalization ability: A hybrid framework for modelling the annual dynamics of satellite-derived land surface temperatures. ISPRS J. Photogramm. Remote Sens. 151, 189–206.

Machado, L., Laurent, H., Dessay, N., Miranda, I., 2004. Seasonal and diurnal variability of convection over the Amazonia: A comparison of different vegetation types and large scale forcing. Theor. Appl. Climatol. 78 (1–3), 61–77.

Manoli, G., Fatichi, S., Schläpfer, M., Yu, K., Crowther, T.W., Meili, N., Bou-Zeid, E., 2019. Magnitude of urban heat islands largely explained by climate and population. Nature 573 (7772), 55–60.

Manoli, G., Fatichi, S., Bou-Zeid, E., Katul, G.G., 2020. Seasonal hysteresis of surface urban heat islands. Proc. Natl Acad. Sci. USA 117 (13), 7082–7089.

Meng, L., Mao, J., Zhou, Y., Richardson, A.D., Lee, X., Thornton, P.E., Ricciuto, D.M., Li, X., Dai, Y., Shi, X., Jia, G., 2020. Urban warming advances spring phenology but reduces the response of phenology to temperature in the conterminous United States. Proc. Natl Acad. Sci. USA 117 (8), 4228–4233.

Oke, T.R., 1973. City size and the urban heat island. Atmos. Environ. 7 (8), 769–779.

Oke, T.R., Mills, G., Christen, A., Voogt, J., 2017. Urban climate. Cambridge University Press.

Peng, S., Piao, S., Ciais, P., Friedlingstein, P., Ottle, C., Bréon, F.-M., Nan, H., Zhou, L., Myneni, R.B., 2012. Surface urban heat island across 419 global big cities. Environ. Sci. Technol. 46 (2), 696–703.

Román, M.O., Schaaf, C.B., Lewis, P., Gao, F., Anderson, G.P., Privette, J.L., Strahler, A. H., Woodcock, C.E., Barnsley, M., 2010. Assessing the coupling between surface albedo derived from MODIS and the fraction of diffuse skylight over spatially-characterized landscapes. Remote Sens. Environ. 114 (4), 738–760.
Rousseeuw, P.J., 1987. Silhouettes: A graphical aid to the interpretation and validation of cluster analysis. J. Comput. Appl. Math. 20, 53–65.
Rubel, F., Kottek, M., 2010. Observed and projected climate shifts 1901–2100 depicted by world maps of the Köppen-Geiger climate classification. Meteorologische Zeitschrift 19 (2), 135–141.
Schläpfer, M., Lee, J., Bettencourt, L., 2015. Urban skylines: building heights and shapes as measures of city size. Preprint at https://arxiv.org/abs/1512.00946.
Sismanidis, P., Bechtel, B., Keramitsoglou, I., Göttsche, F., Kiranoudis, C.T., 2021. Satellite-derived quantification of the diurnal and annual dynamics of land surface temperature. Remote Sens. Environ. 265, 112642. https://doi.org/10.1016/j.rse.2021.112642.
Sismanidis, P., Keramitsoglou, I., Kiranoudis, C.T., 2015. Diurnal analysis of surface urban heat island using spatially enhanced satellite derived LST data. In 2015 Joint Urban Remote Sensing Event (JURSE), pp. 1–4.
Streutker, D., 2003. Satellite-measured growth of the urban heat island of Houston, Texas. Remote Sens. Environ. 85 (3), 282–289.
Tran, H., Uchihama, D., Ochi, S., Yasuoka, Y., 2006. Assessment with satellite data of the urban heat island effects in Asian mega cities. Int. J. Appl. Earth Obs. Geoinf. 8 (1), 34–48.
Voogt, J.A., Oke, T.R., 2003. Thermal remote sensing of urban climates. Remote Sens. Environ. 86 (3), 370–384.
Venter, Z.S., Chakraborty, T., Lee, X., 2021. Crowdsourced air temperatures contrast satellite measures of the urban heat island and its mechanisms. Sci. Adv. 7, eabb9569.
Wan, Z., 2008. New refinements and validation of the MODIS land surface temperature/emissivity products. Remote Sens. Environ. 112, 59–74.
Wan, Z., 2014. New refinements and validation of the collection-6 MODIS land-surface temperature/emissivity product. Remote Sens. Environ. 140, 36–45.
Wang, L., Jia, Y., Li, X., Gong, P., 2020. Analysing the driving forces and environmental effects of urban expansion by mapping the speed and acceleration of built-up areas in china between 1978 and 2017. Remote Sen. 12 (23), 3929.
Weng, Q., Fu, P., 2014. Modeling diurnal land temperature cycles over Los Angeles using downscaled GOES imagery. ISPRS J. Photogramm. Remote Sens. 97, 78–88.
Yao, R., Wang, L., Huang, X., Gong, W., Xia, X., 2019. Greening in rural areas increases the surface urban heat island intensity. Geophys. Res. Lett. 46 (4), 2204–2212.
Zakšek, K., Oštir, K., 2012. Downscaling land surface temperature for urban heat island diurnal cycle analysis. Remote Sens. Environ. 117, 114–124.
Zhang, X., Friedl, M.A., Schaaf, C.B., Strahler, A.H., Liu, Z., 2005. Monitoring the response of vegetation phenology to precipitation in Africa by coupling MODIS and TRMM instruments. J. Geophys. Res.-Atmos. 110 (D12103), 1–14.
Zhao, L., Lee, X., Smith, R.B., Oleson, K., 2014. Strong contributions of local background climate to urban heat islands. Nature 511 (7508), 216–219.
Zhou, B., Rybski, D., Kropp, J.P., 2013a. On the statistics of urban heat island intensity. Geophys. Res. Lett. 40 (20), 5486–5491.
Zhou, B., Lauwaet, D., Hooyberghs, H., De Ridder, K., Kropp, J.P., Rybski, D., 2016a. Assessing seasonality in the surface urban heat island of London. J. Appl. Meteorol. Clim. 55 (3), 493–505.
Zhou, B., Rybski, D., Kropp, J.P., 2017. The role of city size and urban form in the surface urban heat island. Sci. Rep. 7 (1), 1–9.
Zhou, J.i., Chen, Y., Wang, J., Zhan, W., 2011. Maximum nighttime urban heat island (UHI) intensity simulation by integrating remotely sensed data and meteorological observations. IEEE J. Sel. Top. Appl. Earth Obs. Remote Sens. 4 (1), 138–146.
Zhou, J.i., Chen, Y., Zhang, X.u., Zhan, W., 2013b. Modelling the diurnal variations of urban heat islands with multi-source satellite data. Int. J. Remote Sens. 34 (21), 7568–7588.
Zhou, D., Xiao, J., Bonafoni, S., Berger, C., Deilami, K., Zhou, Y., Frolking, S., Yao, R., Qiao, Z., Sobrino, J., 2019. Satellite remote sensing of surface urban heat islands: Progress, challenges, and perspectives. Remote Sens. 11 (1), 48. https://doi.org/10.3390/rs11010048.
Zhou, D., Zhang, L., Li, D., Huang, D., Zhu, C., 2016b. Climate–vegetation control on the diurnal and seasonal variations of surface urban heat islands in China. Environ. Res. Lett. 11 (7), 074009. https://doi.org/10.1088/1748-9326/11/7/074009.
Zhou, D., Zhao, S., Liu, S., Zhang, L., Zhu, C., 2014. Surface urban heat island in China's 32 major cities: Spatial patterns and drivers. Remote Sens. Environ. 152, 51–61.